Observing Intermediate-mass Black Holes and the Upper Stellar-mass gap with LIGO and Virgo

Ajit Kumar Mehta[1] , Alessandra Buonanno[1,2] , Jonathan Gair[1] , M. Coleman Miller[3] , Ebraheem Farag[4,5] ,
R. J. deBoer[5,6] , M. Wiescher[5,6] , and F. X. Timmes[4,5]

[1] Max Planck Institute for Gravitational Physics (Albert Einstein Institute), Am Mühlenberg 1, Potsdam D-14476, Germany; ajit.mehta@aei.mpg.de
[2] Department of Physics, University of Maryland, College Park, MD 20742-2421, USA
[3] Department of Astronomy and Joint Space-Science Institute, University of Maryland, College Park, MD 20742-2421, USA
[4] School of Earth and Space Exploration, Arizona State University, Tempe, AZ 85287, USA
[5] Joint Institute for Nuclear Astrophysics—Center for the Evolution of the Elements, USA
[6] Department of Physics, University of Notre Dame, Notre Dame, IN 46556, USA

Abstract

Using ground-based gravitational-wave detectors, we probe the mass function of intermediate-mass black holes (IMBHs) wherein we also include BHs in the upper mass gap at $\sim$60–130 $M_\odot$. Employing the projected sensitivity of the upcoming LIGO and Virgo fourth observing run (O4), we perform Bayesian analysis on quasi-circular nonprecessing, spinning IMBH binaries (IMBHBs) with total masses 50–500 $M_\odot$, mass ratios 1.25, 4, and 10, and dimensionless spins up to 0.95, and estimate the precision with which the source-frame parameters can be measured. We find that, at 2σ, the mass of the heavier component of IMBHBs can be constrained with an uncertainty of $\sim$10%–40% at a signal-to-noise ratio of 20. Focusing on the stellar-mass gap with new tabulations of the ^{12}C$(\alpha, \gamma)^{16}$O reaction rate and its uncertainties, we evolve massive helium core stars using MESA to establish the lower and upper edges of the mass gap as $\simeq 59^{+34}_{-13} M_\odot$ and $\simeq 139^{+30}_{-14} M_\odot$ respectively, where the error bars give the mass range that follows from the $\pm 3\sigma$ uncertainty in the ^{12}C$(\alpha, \gamma)^{16}$O nuclear reaction rate. We find that high resolution of the tabulated reaction rate and fine temporal resolution are necessary to resolve the peak of the BH mass spectrum. We then study IMBHBs with components lying in the mass gap and show that the O4 run will be able to robustly identify most such systems. Finally, we reanalyze GW190521 with a state-of-the-art aligned-spin waveform model, finding that the primary mass lies in the mass gap with 90% credibility.

Unified Astronomy Thesaurus concepts: Gravitational wave astronomy (675); Astronomical methods (1043); Gravitational waves (678)

1. Introduction

The LIGO and Virgo detectors (Aasi et al. 2015; Acernese et al. 2015) have opened the gravitational-wave (GW) window onto the universe, reporting, so far, 48 GW signals from binary black hole (BH) mergers (Abbott et al. 2019a, 2020c). They have also opened the era of multimessenger astronomy with GWs, shedding light on the origin of short–hard gamma-ray bursts with the observation of a coalescing binary neutron star (Abbott et al. 2017a, 2017b). In addition, independent claims of GW observations have also been made (Nitz et al. 2019, 2020; Venumadhav et al. 2020; Zackay et al. 2021). Detections of these compact-object binaries have allowed us to probe various problems pertaining to astrophysics, astronomy, and cosmology, such as measuring the Hubble parameter (Abbott et al. 2017c), establishing the rates and population of compact binaries (Abbott et al. 2021b), and constraining the neutron-star radius and equation of state (Abbott et al. 2018, 2020c). The detections of binary black hole (BBH) mergers with masses $\gtrsim 40 M_\odot$, in particular, can allow us to probe the physical processes that are involved in the evolution of massive stars—for example, the ^{12}C$(\alpha, \gamma)^{16}$O nuclear rate that significantly affects the mass of a BH formed through the collapse of a massive star (Brown et al. 2001; Woosley et al. 2002; Farmer et al. 2020; Woosley & Heger 2021).

The GW detections during the first and second observing runs (O1 and O2) (Abbott et al. 2019a) revealed a population of BBHs with component source masses $\lesssim 50 M_\odot$ and total source mass $\lesssim 84 M_\odot$. These component masses are mostly consistent with the definition of stellar-mass BHs. However, in the first half of the third observing run (O3a), an event (GW190521) (Abbott et al. 2021b, 2021c) was detected with a pre-merger binary total source mass of $\sim 150 M_\odot$ and a remnant source mass of $\sim 140 M_\odot$. The best estimates of the component BH source masses, obtained with quasi-circular spinning, precessing waveforms, are $\sim 85 M_\odot$ and $\sim 65 M_\odot$ (Abbott et al. 2020b). The remnant of this GW event falls in the category of intermediate-mass black holes (IMBHs), which are usually defined as BHs with mass between $\sim 10^2$ and $10^5 M_\odot$. The latter is not a strict definition. Because we are also interested in studying BHs in the upper mass gap (i.e., the gap produced by pair instability supernovae), we define IMBHs as those with masses above the lower edge of this mass gap. As we show in Section 4.3, that lower edge is at $\sim 60 M_\odot$, and thus for our purposes BHs with masses $M \gtrsim 60 M_\odot$ are IMBHs. Minimal-assumption LIGO–Virgo pipelines dedicated to searches for IMBHs have not reported any detection except for GW190521 so far (Abbott et al. 2017d, 2019b).

We note that Nitz & Capano (2021) have recently found evidence, using a waveform model that was not employed in Abbott et al. (2021b, 2021c), that the source-mass posterior distributions of GW190521 are multimodal, opening the possibility that GW190521 was a binary with intermediate mass ratio (i.e., around 10). We will comment on their analysis,
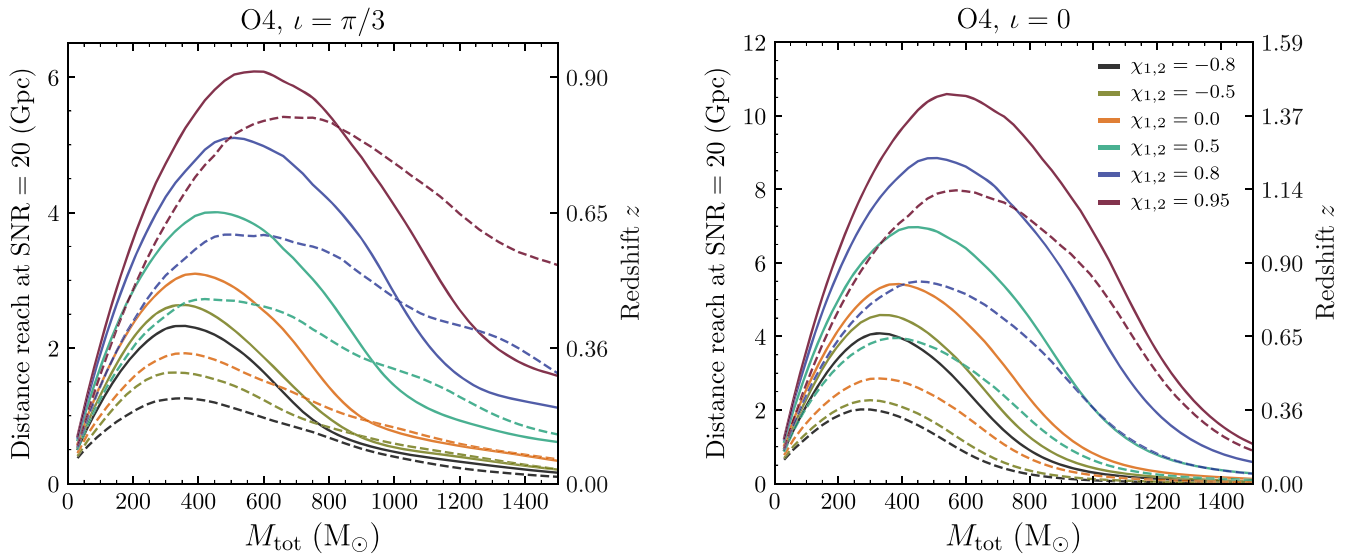
Figure 1. The distance reach as a function of the total mass M_{tot} for spinning, nonprecessing IMBHBs with mass ratio $q = 1.25$ (solid lines) and $q = 4$ (dashed lines) at inclination angle $\iota = \pi/3$ (left panel) and $\iota = 0$ (right panel), and S/N = 20. The different curves correspond to different values of the component spins (χ_1, χ_2), assumed to be equal for the two BHs. We use the noise spectral densities expected for the upcoming O4 run (Abbott et al. 2020a) and the spinning, nonprecessing SEOBNRHM waveform model. The distance reach shown here is computed by averaging over the antenna pattern functions (see Equation (4)), which are the angles that specify the location of the source in the sky and the polarization angle. The maximum redshift (distance reach) for IMBHBs with inclination $\iota = 0$ (face-on) and $\pi/3$ (nearly edge-on) is $z \sim 1.4$ (11 Gpc) and ~ 0.9 (6 Gpc), respectively.

and we reanalyze this GW event as well in Section 4.7 below. A similar conclusion was drawn by Fishbach & Holz (2020), in which the authors employed a different—namely, population-informed—prior on the secondary mass rather than a uniform prior on it. Given the very short signal, other analyses in the literature (Romero-Shaw et al. 2020; Gayathri et al. 2020b; Bustillo et al. 2021; Calderón Bustillo et al. 2021) pointed out the importance of reanalyzing GW190521 with waveform models of eccentric compact binaries, although these are not yet available.

IMBHs are difficult to observe. Indeed, there is no definitive electromagnetic evidence for their existence. Thus, their formation channels and mass function are highly uncertain (Miller & Colbert 2004; Amaro-Seoane et al. 2007; Gair et al. 2011; Belczynski et al. 2014). GW observations have the potential to solve these mysteries, by providing accurate measurements of their properties, such as their masses, spins, and location.

Graff et al. (2015), Veitch et al. (2015a), and Haster et al. (2016) studied the precision with which IMBH masses and spins could be measured with LIGO and Virgo detectors. Graff et al. (2015) used multipolar waveform models that describe the entire coalescence process of nonspinning IMBHBs, and performed a Bayesian analysis to estimate the precision with which the parameters of IMBHBs can be estimated with LIGO detectors. Veitch et al. (2015a) employed spinning, nonprecessing waveforms, but did not include subdominant modes; these are relevant for high total-mass binaries, because they break degeneracies between parameters and reduce the measurement uncertainties. Here we extend these analyses in several directions. We consider state-of-the-art multipolar spinning, nonprecessing models for gravitational waves from IMBHBs, including the five strongest gravitational modes, and explore a larger region of the parameter space (e.g., mass ratios 1–10 and dimensionless spin values up to 0.95). We focus on masses in the source frame rather than the detector frame, since the former provide us with information about the upper stellar-mass gap and more generally about the IMBH mass function.

We employ for our study the projected noise spectral densities (Abbott et al. 2020a) of the upcoming fourth observing run (O4) (scheduled to start not earlier than the second half of 2022). We also comment on results that could be obtained during the fifth observing run (O5) (Abbott et al. 2020a) (expected to start in 2025).

Inference on the IMBH population requires not only accurate parameter measurements, but also a sufficiently high rate of observations of IMBHB mergers in upcoming LIGO and Virgo runs (see Ezquiaga & Holz 2021 for a study when the BH masses are above 120 $M_\odot$). Based on the observation of one event, GW190521, Abbott et al. (2020c) estimated an astrophysical merger rate of $0.13^{+0.30}_{-0.11}$ Gpc^{-3} yr^{-1}. In Figure 1, we show the distance reach of the LIGO–Virgo detector network expected during O4 to binaries with signal-to-noise ratio (S/N) of 20. We display results using multipolar spinning, nonprecessing waveforms, for a variety of spin values and for mass ratios of 1.25 and 4, and binary inclinations $\iota = 0$ (face-on) and $\iota = \pi/3$ (close to edge-on). As we can see, the distance reach for face-on binaries even at S/N = 20 could go up to a redshift $z \sim 1.4$ (11 Gpc), while for nearly edge-on binaries this reduces a bit, but sources at a redshift of ~ 0.9 (6 Gpc) can still be probed. When combined with the measured astrophysical rate, this distance reach implies that we could expect a detection rate as high as $\sim 43^{+185}_{-36}$ yr^{-1} for face-on binaries and $\sim 21^{+92}_{-18}$ yr^{-1} for nearly edge-on IMBH binaries with S/N ~ 20 at O4 sensitivity. At O5 sensitivity at the same S/N, the maximum redshift reach for face-on binaries can go up to ~ 2.5, while for nearly edge-on binaries it is ~ 1.6 (Figure 2). The previous numbers then increase to $\sim 116^{+500}_{-98}$ yr^{-1} and $\sim 55^{+235}_{-46}$ yr^{-1}. We note that these numbers assume a fixed model for the mass distribution of IMBHBs and the evolution of the rate density with redshift, neither of which has been constrained by previous observations. The uncertainties are therefore underestimated.

As said earlier, inferring IMBH parameters and estimating the corresponding measurement uncertainties will have important implications for understanding the formation of high-mass BHs and the evolution of massive stars. The theory of stellar evolution predicts that stars with zero-age main-sequence (ZAMS) masses $100\,M_\odot \lesssim M_{\rm ZAMS} \lesssim 130\,M_\odot$ are subject to pair instability (Fowler & Hoyle 1964; Barkat et al. 1967; Rakavy & Shaviv 1967), which causes the stars to lose mass and leave behind a remnant with a typical mass smaller than $\sim 65\,M_\odot$ (Heger et al. 2003; Blinnikov 2010; Chatzopoulos & Wheeler 2012; Yoshida et al. 2016; Woosley 2017; Umeda et al. 2020). These events set the lower edge of the BH mass gap.

Stars with masses $130\,M_\odot \lesssim M_{\rm ZAMS} \lesssim 250\,M_\odot$ are subject to the pair instability, which disrupts them completely, and hence no BH forms. Stars with $M_{\rm ZAMS} \gtrsim 250\,M_\odot$ can collapse directly to IMBHs with a mass $\gtrsim 135\,M_\odot$. Thus, in the standard picture, there should be an upper stellar-mass BH gap in the range [65, 135] $M_\odot$, and any BHs observed in this range (e.g., the primary BH of GW190521) have to form via other formation channels—for example, through hierarchical coalescence of smaller BHs or direct collapse of a stellar merger between an evolved star and a main-sequence companion (e.g., Quinlan & Shapiro 1989; Portegies Zwart & McMillan 2000; Ebisuzaki et al. 2001; Miller & Hamilton 2002; O'Leary et al. 2006; Gerosa & Berti 2017; Antonini et al. 2019; Di Carlo et al. 2019, 2020; Rodriguez et al. 2019; Gayathri et al. 2020a; Kimball et al. 2021; Mapelli et al. 2021). However, the exact mass boundaries of the gap depend on parameters that are uncertain. For example, the $^{12}{\rm C}(\alpha, \gamma)^{16}{\rm O}$ nuclear reaction rate, which converts carbon to oxygen in the core, can affect the boundary significantly (Takahashi 2018; Farmer et al. 2020; Costa et al. 2021; Woosley & Heger 2021). Here, to better determine whether future GW observations will be able to observe BHs in the mass gap, we recompute the mass-gap boundaries with updated $^{12}{\rm C}(\alpha, \gamma)^{16}{\rm O}$ reaction rates and increased mass and temporal resolution. The complexity of this system has made a reliable analysis of the reaction a decades-old challenge.[7] The rapidly declining cross section at low energies has prohibited a direct measurement of the reaction at stellar temperatures, and the reaction rate is entirely based on the theoretical analysis and extrapolation of the experimental data toward lower energies. The rate newly derived by deBoer et al. (2017), using a multichannel analysis approach, derives for the first time a reliable prediction for the interference patterns within the reaction components by taking into account all available experimental data sets that cover the near-threshold energy range of the $^{12}{\rm C}(\alpha, \gamma)^{16}{\rm O}$ process.

The paper is organized as follows. In Section 2 we introduce the gravitational waveform models that we employ for our parameter-estimation studies, and briefly review the Bayesian analysis method that we use to infer the source properties from the GW signals. In Section 3 we first describe the parameter space of the binary simulations that we investigate and the

choice of priors. Then, we present the results for the expected measurement uncertainties that could be obtained with observations made during the LIGO–Virgo O4 run and also comment on results that could be obtained during the O5 run. We also discuss the bimodality that appears in the posterior distributions for some parameters in some regions of the parameter space. In Section 4, after a brief review of the BH mass gap and a discussion of the current estimate of the $^{12}{\rm C}(\alpha, \gamma)^{16}{\rm O}$ reaction rates, we evolve massive He stars by incorporating new uncertainties in the nuclear reaction rates and we establish new bounds on the lower and upper edges of the mass gap. Then, using these results, we estimate the probability with which LIGO–Virgo O4 and O5 runs can identify IMBHB systems whose primary and secondary masses lie in the BH mass gap. We also reanalyze GW190521 with the spinning, nonprecessing waveform models employed in this work, and find that, although a bimodality in the posterior distributions of the detector-frame masses is present, it is absent from the posteriors of the source-mass parameters. To contrast these findings with precessing waveforms, we also analyze GW190521 with one precessing waveform model, whose former public version was employed in Nitz & Capano (2021). Finally, in Section 5, we present our main conclusions and discuss possible future research directions.

2. Setup

2.1. Waveform Models

We focus our study on GW signals generated by BBHs with nonprecessing spins, moving on quasi-circular orbits. Such signals are described by 11 parameters: $\boldsymbol{\theta} \equiv \{m_1, m_2, \chi_1, \chi_2, d_L, t_c, \delta, \alpha, \iota, \psi, \phi_c\}$. The parameters $m_{1,2}$ are the redshifted (i.e., detector-frame) component masses $m_i = (1 + z)m_i^s$ for $i = 1, 2$, where m_i^s is the source-frame mass and z the redshift. The quantities $\chi_{1,2}$ are the dimensionless component spins along the orbital angular momentum $\boldsymbol{L}$ of the binary (i.e., $\chi_i = \boldsymbol{S}_i \cdot \boldsymbol{L}/m_i^2$ for $i = 1, 2$). The parameter d_L is the luminosity distance to the binary, which along with the decl. δ and the R.A. α defines the location of the binary in the sky. The parameter t_c is the merger time or more specifically, it is the peak time of the $\ell = 2, m = 2$ gravitational mode at the geocenter. The angle ι measures the inclination of the binary's total angular momentum $\boldsymbol{J}$ (which, for nonprecessing binary systems, has the same direction as the orbital angular momentum $\boldsymbol{L}$) with respect to the line of sight from the detector at the geocenter. The remaining parameters ϕ_c and ψ are the merger phase and the gravitational wave polarization, respectively.

It is also useful to define the following binary parameters: the total mass $M_{\rm tot} = m_1 + m_2$, the mass ratio $q = m_1/m_2 \geqslant 1$, the symmetric mass ratio $\nu = q/(1 + q)^2$, the chirp mass $M_c = M_{\rm tot}\nu^{3/5}$, and the effective spin of the binary $\chi_{\rm eff} = (m_1\chi_1 + m_2\chi_2)/M_{\rm tot}$.

In general relativity, GWs are described by the two polarizations $h_+(t)$ and $h_\times(t)$. The complex waveform defined by $h(t) \equiv h_+(t) - ih_\times(t)$ can be conveniently decomposed in a basis of -2 spin-weighted spherical harmonics (Pan et al. 2011):

$$h(t; \boldsymbol{\lambda}, \iota, \varphi_c) = \frac{1}{d_L}\sum_{\ell \geqslant 2}\sum_{|m| \leqslant \ell} {}_{-2}Y_{\ell m}(\iota, \varphi_c)\, h_{\ell m}(t, \boldsymbol{\lambda}), \qquad (1)$$

---

[7] The reaction rate for $^{12}{\rm C}(\alpha, \gamma)^{16}{\rm O}$ is determined by the quantum structure of the compound nucleus $^{16}{\rm O}$ as an α cluster system. It is characterized by the interfering $\ell = 1$ waves of the $J^\pi = 1^-$ resonances and sub-threshold levels defining an E1 component for the reaction cross section as well as by the $\ell = 2$ components and interference from broad $J^\pi = 2^+$ resonances and the nonresonant E2 external capture to the ground state of $^{16}{\rm O}$. In addition to these two main E1 and E2 ground-state components, transitions to higher lying excited states occur that also add to the total cross section (see, e.g., Buchmann & Barnes 2006; deBoer et al. 2017).
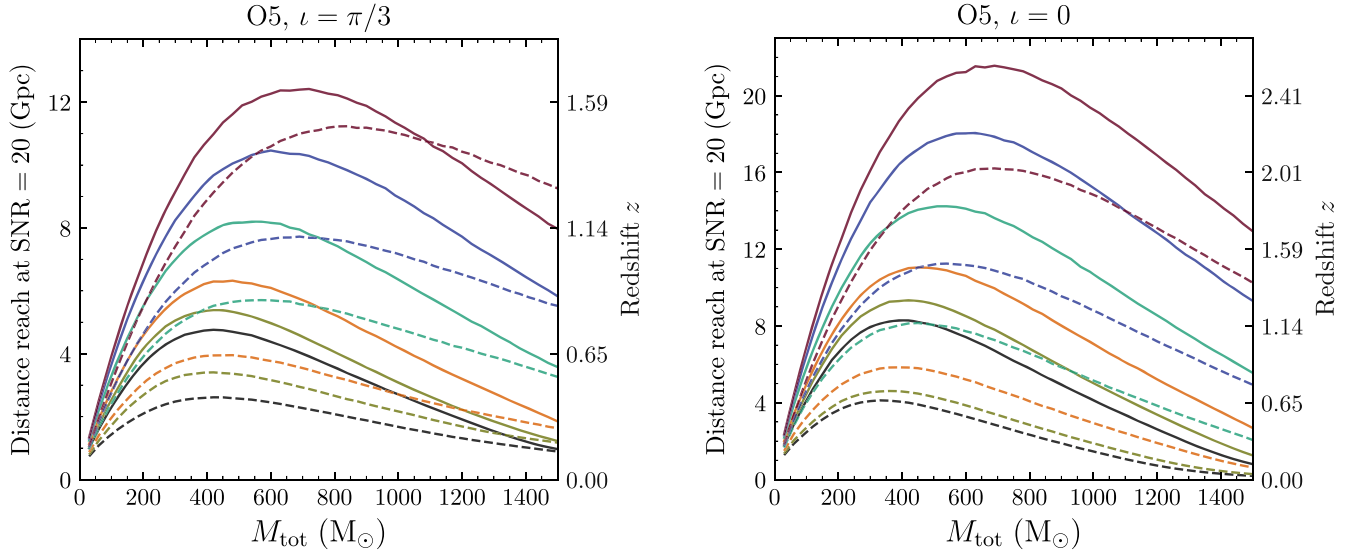
Figure 2. Same as Figure 1 but for the noise spectral densities of the O5 run (Abbott et al. 2020a). The maximum redshift (distance reach) for IMBHBs with inclination $\iota = 0$ (face-on) and $\pi/3$ (nearly edge-on) is $z \sim 2.5$ (20.9 Gpc) and ~ 1.6 (12.1 Gpc), respectively.

where λ denotes a subset of the θ parameters, namely, the intrinsic parameters of the binary systems such as masses (m_1, m_2) and spins (χ_1, χ_2).

The GW signal emitted throughout the coalescence of a BBH can be divided into three phases: inspiral, merger, and ringdown (IMR). The inspiral phase describes the steady, adiabatic evolution of the system where the component BHs come closer and closer to each other, losing orbital energy because of GW emission. At the end of the inspiral, the BHs plunge into each other, form a common apparent horizon, and merge. The ringdown phase describes the evolution of the system as the remnant object settles down to a stationary (Kerr) BH.

Here, we employ, as the main IMR waveform model, the one developed within the effective one-body formalism (EOB), which is a semianalytical method that combines results from post-Newtonian (PN) theory for the inspiral, BH perturbation theory for the ringdown, and numerical relativity (NR) for the merger stage. More specifically, since we are interested in studying high-mass BBHs with mass ratio as large as 10, we employ the quasi-circular, nonprecessing spinning waveform models with gravitational modes beyond the dominant, quadrupolar one (Cotesta et al. 2018) (henceforth, SEOBNRHM).[8] The SEOBNRHM model contains the five strongest modes (ℓ, m) = (2, $\pm$1), (2, $\pm$2), (3, $\pm$3), (4, $\pm$4), (5, $\pm$5) (see Equation (1)). We also use for synthetic (injection) signals a spinning, precessing IMR model built directly by interpolating NR waveforms NRSurPHM (Varma et al. 2019a).[9] Such a model contains all modes with $\ell \leqslant 5$. However, the extra modes present in NRSurPHM and absent from SEOBNRHM are not expected to contribute significantly to our choices of parameters. Finally, we also use a phenomenological IMR waveform model built in the frequency domain by combining EOB and NR waveforms, PhenomHM (García-Quirós et al. 2020).[10] We stress that, in general, the higher-order (or

subdominant) modes become important in the parameter estimation of the binaries when the inclination angle is large and the mass ratio is large, $q \equiv m_1/m_2 \geqslant 1$ (see, e.g., Cotesta et al. 2018). Moreover, higher total mass and higher spins also increase the amplitude of subdominant modes, especially close to the merger of the binary. We will see in Sections 3.2 and 3.3 that higher modes can be important to precisely infer the parameters even when the mass ratio is as low as $q \sim 1.25$, but the total mass and/or the spins are high.

2.2. Bayesian Statistics

Bayes' theorem allows us to construct the probability distribution of parameters θ given a hypothesis (or a model) $\mathcal{H}$ and a data set d. It states

$$P(\theta|d, \mathcal{H}) = \frac{P(d|\theta, \mathcal{H})P(\theta|\mathcal{H})}{P(d|\mathcal{H})}, \quad (2)$$

where $P(\theta|d, \mathcal{H})$ is the posterior probability distribution of parameters θ, given a data set d, under the hypothesis $\mathcal{H}$. The quantity $P(\theta|\mathcal{H})$ in Equation (2) is the prior probability distribution of the parameters θ under the hypothesis $\mathcal{H}$. The function $P(d|\theta, \mathcal{H})$ is the likelihood (very often denoted as $\mathcal{L}(\theta)$) of obtaining the data set d with a specific parameter set θ, under the hypothesis $\mathcal{H}$. Bayes' theorem updates our prior knowledge of the parameters using the likelihood of the data to finally provide us with the posterior probability distribution. Lastly, the quantity $P(d|\mathcal{H})$ in Equation (2) is known as the evidence for the data set d under the hypothesis $\mathcal{H}$. It is the normalization factor of the posterior probability distribution in Equation (2) and thus it does not matter in our parameter-estimation study. It is, however, widely used for comparing different hypotheses.

In this work, we assume that we have already detected a GW signal and our job is to extract the parameters that describe this signal most closely. The data output from the GW detectors can be written as follows (under the assumption of additive noise):

$$d = n + h, \quad (3)$$

---

[8] In the LIGO Algorithm Library (LAL) the technical name of this waveform model is SEOBNRv4HM_ROM. It is the reduced-order model (ROM) of the time-domain waveform model SEOBNRv4HM (Cotesta et al. 2018, 2020).
[9] In LAL this waveform model is denoted NRSur7dq4 (Varma et al. 2019a).
[10] In LAL this waveform model is denoted IMRPhenomXHM (García-Quirós et al. 2020).

where n represents the noise realization from the GW detectors and h is the GW strains measured at the different detectors. Here

$$h = F_+(\alpha, \delta, \psi)h_+ + F_\times(\alpha, \delta, \psi)h_\times, \qquad (4)$$

where $F_{+,\times}(\alpha, \delta, \psi)$ denote the antenna pattern functions (Finn & Chernoff 1993) that account for the angular sensitivity of the GW detectors and thus depend on the source location (α, δ), and on the polarization angle, ψ, that defines the relative orientation of the polarization axes with respect to which the polarization states $h_{+,\times}$ are defined. To construct the posterior distribution of parameters $\boldsymbol{\theta}$, which describe the GW signal h, we must first write down the likelihood function.

2.2.1. Likelihood Function

Let d_a denote a data stream in a particular detector a. Then the likelihood $\mathcal{L}_a(\boldsymbol{\theta})$ or $P(d_a|\boldsymbol{\theta}, \mathcal{H}_S)$ is, by definition, the probability of obtaining the data d_a with a specified set of parameters $\boldsymbol{\theta}$. Thus, for a GW signal $h_a(\boldsymbol{\theta})$, the likelihood should be given by the probability of observing the noise realization, $n_a = d_a - h_a(\boldsymbol{\theta})$. The noise realizations in GW detectors are modeled as independent Gaussian distributions in each frequency bin with a zero mean and a variance given by the detector's power spectral density (PSD). Thus, up to an additive constant,

$$\log \mathcal{L}_a(\boldsymbol{\theta}) \propto -\frac{1}{2}\sum_i \left[\frac{4}{T_a} \frac{|\tilde{d}_a(f_i) - \tilde{h}_a(f_i, \boldsymbol{\theta})|^2}{S_n^{(a)}(f_i)} \right], \qquad (5)$$

where i runs over each frequency bin, T_a is the duration of the GW signal in detector a, and a tilde represents the Fourier transform of the data series. Here $S_n^{(a)}(f)$ is the (one-sided) noise PSD associated with the detector a. Equation (5) is the discrete approximation to the inner product between the data d and the waveform model (or template) h, denoted by (d, h), where

$$(d, h) \equiv 4\,\mathrm{Re}\int_{f_{min}}^{f_{max}} df \frac{\tilde{d}(f)\tilde{h}^*(f)}{S_n(f)}, \qquad (6)$$

the asterisk denotes the complex conjugate, and f_{min} and f_{max} are the minimum and maximum frequencies over which the integration is performed. Generally, the frequency limits are different for different detectors. S/N of a signal h is defined as $\sqrt{(h, h)}$.

The overlap between two signals h_1 and h_2 is

$$\mathcal{O}_{12} = \max_{t_c, \phi_c} \left[\frac{(h_1, h_2)}{\sqrt{(h_1, h_1)(h_2, h_2)}} \right]. \qquad (7)$$

By definition, the overlap varies between 0 and 1, with the latter representing the case when the two signals are scaled versions of each other.

Assuming that the data streams in the different detectors are independent, we can construct the total log-likelihood function by summing the individual log-likelihoods of the detectors, that is

$$\log \mathcal{L}(\boldsymbol{\theta}) = \sum_a \log \mathcal{L}_a(\boldsymbol{\theta}). \qquad (8)$$

From Equation (8), one can show that the total S/N from all the detectors is the sum in quadrature of the individual S/Ns,

$$\rho = \sqrt{\rho_1^2 + \rho_2^2 + ... b + \rho_N^2}, \qquad (9)$$

where ρ_a represents the S/N of a signal in detector a, and N is the number of detectors.

In this work, when we evaluate Equations (5)–(9), we use $f_{min} = 11$ Hz, and we set f_{max} to half the sampling frequency, which is 4096 Hz. For the results displayed in figures and tables, we use the projected PSDs of the LIGO–Virgo detector network for the upcoming O4 run (Abbott et al. 2020a). We also regenerated most of the results with O5 PSDs (Abbott et al. 2020a) at the same S/N. The duration of the signal T_a in Equation (5) is chosen to vary between 4 s and 128 s depending on the total mass of the simulated BBH system.

2.2.2. Priors

In order to construct the posterior distribution of the parameters $\boldsymbol{\theta}$ using Equation (2), we also need to specify our prior probability distribution $P(\boldsymbol{\theta}|\mathcal{H})$.

For our analysis, we assume a flat prior in the component (detector-frame) masses $m_{1,2} \in [1, 600]\, M_\odot$ with $m_1 \geqslant m_2$. For the location of the binary in the sky, we use flat priors in $\cos\delta$ and α with $\delta \in [0, \pi]$ rad and $\alpha \in [0, 2\pi]$ rad. We assume an isotropic distribution for the orientation of the binary with respect to the observer. This implies that the orientation-angle priors are flat in $\cos(\iota)$ for $\iota \in [0, \pi]$ rad, and flat in ψ and ϕ_c for $\psi \in [0, \pi]$ rad and $\phi_c \in [0, 2\pi]$ rad. The priors for the dimensionless spins, $\chi_{1,2}$, are chosen to follow a uniform distribution between -0.99 and 0.99.

We make use of two distinct distance priors: (i) uniform in Euclidean volume (i.e., flat in d_L^2), and (ii) uniform in comoving volume (V_c), i.e.,

$$P(d_L) \propto \frac{1}{1 + z}\frac{dV_c}{dz}\left(\frac{dd_L}{dz}\right)^{-1}, \qquad (10)$$

where the conversion from redshift, z, to luminosity distance, d_L, depends on the cosmology under consideration. In this work, we use the standard ΛCDM model of the universe (Planck Collaboration et al. 2016). For a spatially flat universe, we have

$$\frac{dd_L}{dz} = d_C + (1 + z)\frac{d_H}{E(z)}, \qquad (11)$$

where d_C is the comoving distance, $d_H = c/H_0$ is the Hubble distance, and $E(z)$ is the normalized Hubble parameter at the redshift z. For both distance priors, we have $d_L \in [100\,\mathrm{Mpc}, 12\,\mathrm{Gpc}]$. By inverting Equation (11), we can obtain the redshift of the source for a given luminosity distance d_L. The source-frame masses are obtained from the detector-frame masses via $m^s = m/(1 + z)$.

To sample the posterior distribution we use the LALINFERENCENEST code (Veitch et al. 2015b). This is a software package for sampling posterior distributions of the parameters of compact-binary GW sources that is part of LAL. It uses nested sampling to explore the posterior distribution. Nested sampling (Skilling 2006) was originally introduced as an efficient way to compute the Bayesian evidence, as a tool for model selection, but also returns independent samples from the posterior distribution on the parameters. The algorithm evolves
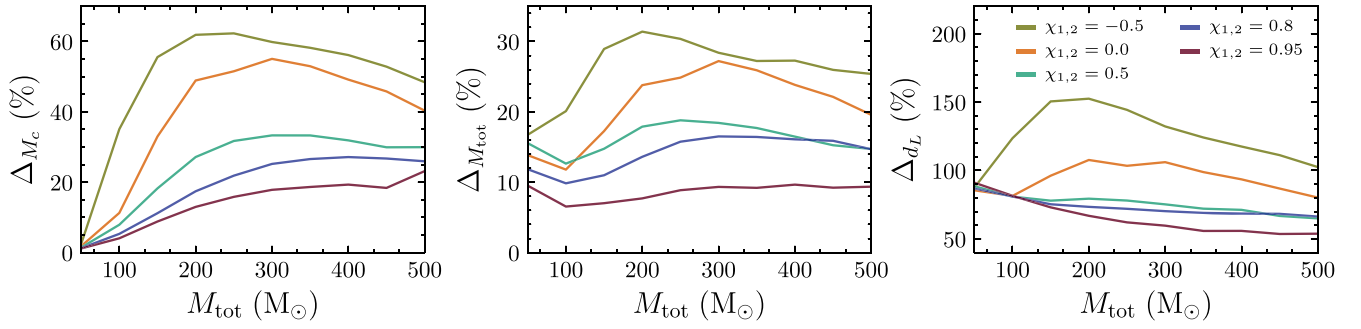
Figure 3. The 95% relative width in the measurement of the parameters $\Theta = \{M_c, M_{tot}, d_L\}$ defined by $\Delta_\Theta = \Delta\Theta^{95\%}/\Theta^{inj} \times 100$, where $\Delta\Theta^{95\%}$ is the 95% absolute width and Θ^{inj} is the true value of the parameter Θ. These results correspond to spinning, nonprecessing BBH systems with $q = 4$, $\iota = \pi/3$ at S/N = 20. The different colored lines represent the different values of component spins (with $\chi_1 = \chi_2$), as illustrated in the legend in the rightmost plot. We use SEOBNRHM waveforms for the injection and recovery. For $\chi_1 = \chi_2 = 0.95$ systems, the worsening in the precision of the chirp mass (left panel) for $M_{tot} \geqslant 450\ M_\odot$ is due to the occurrence of bimodality in the posterior of M_c.

a set of *live points*, replacing the point with the lowest likelihood at each step by another point of higher likelihood chosen uniformly from the prior distribution. The LALINFER-ENCENEST code achieves these updates using short Markov Chain Monte Carlo evolutions. We refer the reader to Veitch et al. (2015b) for further details of the implementation.

3. Measurement of IMBH Properties

3.1. Parameter Space of Simulations

To understand the uncertainty with which the parameters of GW signals from IMBHBs could be constrained with upcoming observations (Abbott et al. 2020a), we simulate a set of (synthetic) GW events and analyze them using Equation (2). For simplicity, the signals are simulated (injected) in a zero-noise background. The addition of noise is expected mainly to change the peak of the posteriors not the widths (or the uncertainties), which are our primary interest. Unless otherwise stated, we choose simulated signals that have LIGO–Virgo network S/N of 20. The event GW190521 was observed with S/N $\approx$ 15 (Abbott et al. 2021b, 2021c), so with the improved sensitivity expected in O4, seeing similar events at S/N $\sim$ 20 is not unreasonable. Higher S/N events will provide the best parameter estimates and hence are those that are most likely to be confidently identified as IMBHs.

We work with IMBHBs with mass ratios $q = 1.25$, $q = 4$, and $q = 10$. Based on the trend that we observe in the results, we expect that for any other mass ratio between them, the associated uncertainty is contained within the uncertainties of these three mass ratios. We fix the inclination angle to 60° (i.e., $\iota = \pi/3$) and 0° (face-on). We vary the (detector-frame) total mass in the range $M_{tot} \in [50, 500]\ M_\odot$ with steps of 50 $M_\odot$. Given that we still do not know very accurately the spin distribution for IMBHs, we choose a very wide range of values for the component spins, namely, $\chi_1 = \chi_2 = \{-0.8, -0.5, 0, 0.5, 0.8, 0.95\}$. For the same reason, we also explore binaries with opposite spins—for example, $\chi_1 = 0.5$, $\chi_2 = -0.5$. We find that the results are contained within the range of results set by the equally spinning binaries.

3.2. Results Using Bayesian Analysis

As a cross-check of our analysis, we start our study by reproducing the results of Graff et al. (2015). They focused on IMBHBs with (detector-frame) total masses in the range [50, 500] $M_\odot$, mass ratios $q = 1.25$ and $q = 4$, and S/N = 12 and

used a version of the LIGO noise spectral density at design sensitivity available at that time. They employed for the Bayesian analysis the multipolar nonspinning waveforms, EOBNRHM (Pan et al. 2011).[11] Using our waveform model SEOBNRHM in the nonspinning limit, we could recover the results of Graff et al. (2015) with some small differences—for example, we find that the maximum discrepancy (i.e., the absolute difference between the estimated precisions) is 8% in M_c and ν for high total masses ($M_{tot} \gtrsim 300\ M_\odot$), where the merger and ringdown phases of the signal dominate in the most sensitive frequency band of the detectors. These discrepancies are mainly due to differences between the waveform models. The waveform model used in this work (Cotesta et al. 2018, 2020) is more accurate than the one employed in Graff et al. (2015), since it was calibrated to a much larger set of NR simulations and contains more information from PN theory.

As described in Section 3.1, here we extend the study of Graff et al. (2015) in several directions. We consider multipolar spinning, nonprecessing IMBHB systems with (detector-frame) total masses in the range [50, 500] $M_\odot$, but mass ratios up to 10 (i.e., $q \in [1.25, 10]$) and S/N = 20. We also use updated LIGO and Virgo PSDs, notably the ones for the upcoming O4 and O5 runs (Abbott et al. 2020a). In Figures 3, 4, 5, and 6 we summarize our results for mass ratios $q = 1.25$ and $q = 4$, inclination $\pi/3$, and a variety of spin values, $\chi_1 = \chi_2 = -0.8$, $-0.5, 0, 0.5, 0.8, 0.95$, while in Tables 1, 2, and 3, we provide results for zero inclination (i.e., face-on configuration) and for larger mass ratio (i.e., $q = 10$). Furthermore, we do not show the $\chi_1 = \chi_2 = -0.8$ results in our figures because they sometimes have much higher posterior widths than the other cases owing to their very small number of GW cycles in the detectors' bandwidth. The results also depend on the specific prior choices on the luminosity distance—for example, priors flat in d_L^2 or flat in the comoving volume produce noticeably different results for higher total masses. For all other spin configurations, we do not see any significant differences between the results of the two distance priors. In all figures and tables we display results with a prior flat in comoving volume.

Figure 3 shows the 95% relative widths of the posteriors of different parameters of the binary systems with mass ratio $q = 4$ and several choices for the BH spins. It can be seen that all the systems at the lowest total mass (i.e., $M_{tot} = 50\ M_\odot$) provide measurement of the chirp mass (M_c) better than the total mass. This is because the waveform from the systems at

---

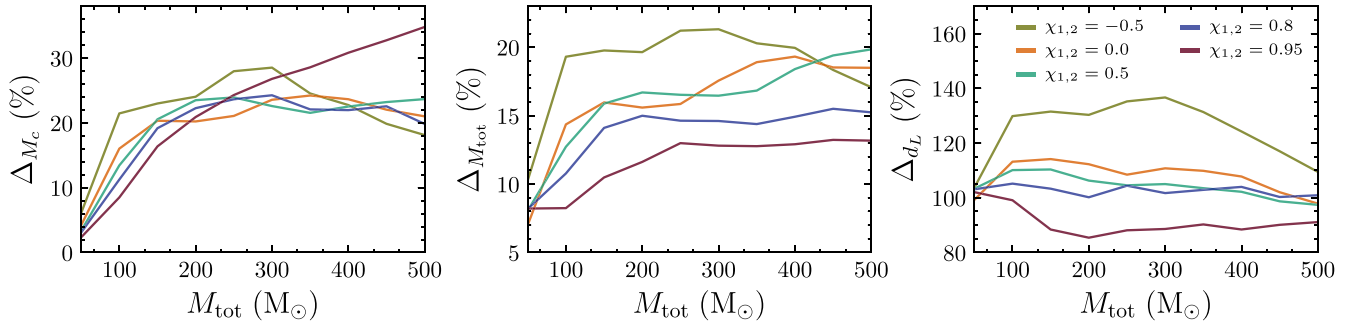[11] In LAL this waveform model is denoted EOBNRv2HM (Pan et al. 2011).

Figure 4. The 95% relative widths in the measurement of the parameters for the binaries with mass ratio $q = 1.25$. The definitions are the same as in Figure 3. For $\chi_1 = \chi_2 = 0.95$ systems, the worsening in the precision of the chirp mass, due to bimodality, starts at $M_{tot} \sim 250\ M_\odot$.
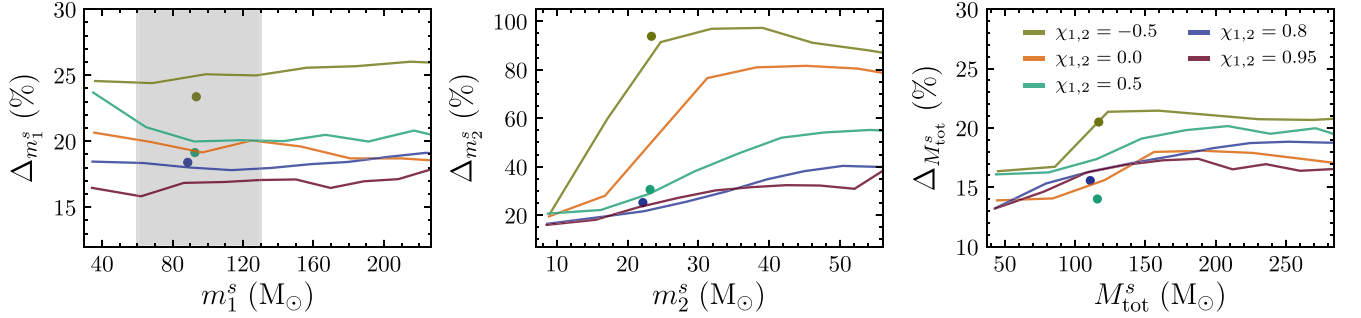

Figure 5. The 95% relative width in the measurement of the source-frame masses $\{m_1^s, m_2^s, M_{tot}^s\}$ of the injected signals from Figure 3 (i.e., for $q = 4$). The upper limits of the x-axes are restricted to the final source-frame masses associated with $\chi_1 = \chi_2 = 0.95$ IMBHB systems, which, because of higher amplitude and hence higher redshift reach, provide the smallest source-frame mass for a given detector-frame mass (e.g., at $M_{tot} = 500\ M_\odot$). The shaded region represents the BH's mass gap of $[60, 130]\ M_\odot$ derived in Section 4.2 and computed at the median ($\sigma = 0$) of the ^{12}C$(\alpha, \gamma)^{16}$O reaction rate (see Figure 10). The dots represent the uncertainties when we inject spinning, precessing signals NRSurPHM, and recover them with spinning, nonprecessing SEOBNRHM waveforms. The 95% uncertainty of each dot should be compared to that of the curve with the same color at the same value of the source-frame parameter. The primary mass can be estimated with a precision $\sim$15%–25% while the total mass can be estimated with a slightly better precision $\sim$12%–22%.

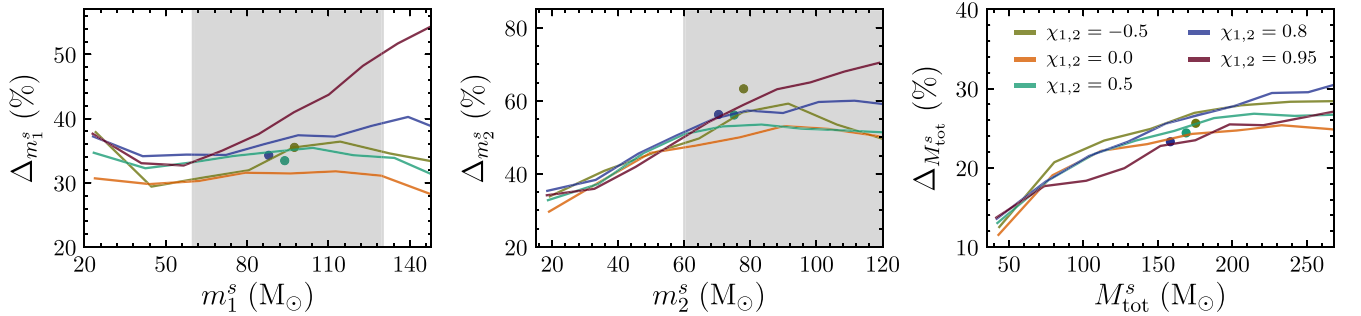**Figure 6.** The 95% relative width in the measurement of the source-frame masses $\{m_1^s, m_2^s, M_{tot}^s\}$ of the injected signals from Figure 4 (i.e., for $q = 1.25$). The other definitions are the same as in Figure 5. Even for symmetric IMBHBs, the primary mass (total mass) can still be estimated with a precision better than 40% (30%) except when spins are high ($\chi_1 = \chi_2 > 0.8$), for which bimodality occurs.

such a low total mass is dominated by its inspiral phase in the most sensitive frequency band of the detectors. At leading PN order, the phase of inspiral gravitational waveforms depends only on the chirp mass M_c (Sathyaprakash & Dhurandhar 1991). At higher total mass, the waveform is dominated by its post-inspiral phase (i.e., by the merger), which is better described by M_{tot}, and thus measures the total mass better (Graff et al. 2015). We find that the total mass at which M_{tot} starts to be measured better than M_c depends also on the spins of the components. We note that mergers of binaries with component spins aligned (antialigned) in the direction of the orbital angular momentum L are delayed (accelerated) compared to their nonspinning counterparts (Campanelli et al. 2006), and thus the binary remains in the inspiral phase longer (shorter) than the nonspinning systems. For example, at $M_{tot} \sim 100\ M_\odot$, the

aligned-spin systems provide more precise measurements of the chirp mass than the total mass, whereas the antialigned-spin systems (see, e.g., the magenta curve) provide more precise measurements of M_{tot}. For $M_{tot} \gtrsim 150\ M_\odot$ onward, regardless of the spin magnitude and orientation, all systems provide more precise measurements of total mass than chirp mass.

As can be seen from Figure 3, the precision of the chirp mass (M_c) measurement initially degrades as the total mass is increased, before starting to improve for sufficiently high masses. The initial increase in the uncertainties is because of the decrease in the number of GW cycles as we increase the total mass of the systems. However, after a certain total mass (depending on the spins), the uncertainty starts to decrease as the merger–ringdown phase of the waveform starts to match well with the minimum of the PSDs, and also the subleading

Table 1
The 95% Width (as a Percentage) of One-dimensional Marginalized Posteriors Scaled by the True Value for Injections and Recoveries with SEOBNRHM Waveforms

Spin	$M_{tot} = 50\ M_\odot$	$100\ M_\odot$	$150\ M_\odot$	$200\ M_\odot$	$250\ M_\odot$	$300\ M_\odot$	$400\ M_\odot$	$500\ M_\odot$
				$\Delta M_c/M_c$				
−0.80	6.53 (6.69)	13.76 (14.85)	23.65 (25.91)	38.73 (38.79)	44.03 (40.90)	47.66 (44.36)	43.84 (39.59)	35.97 (36.33)
−0.50	6.08 (6.11)	21.45 (20.69)	22.99 (23.35)	24.03 (26.60)	27.97 (30.15)	28.52 (32.96)	22.75 (34.83)	18.11 (31.63)
0.00	4.20 (4.18)	16.02 (16.33)	20.32 (20.85)	20.22 (22.43)	21.07 (22.91)	23.56 (25.01)	23.64 (25.95)	21.00 (26.02)
0.50	3.33 (3.30)	13.43 (13.44)	20.55 (20.62)	23.49 (23.58)	23.93 (24.49)	22.59 (23.68)	22.52 (23.53)	23.66 (24.29)
0.80	3.08 (3.02)	11.25 (10.95)	19.18 (18.55)	22.26 (22.20)	23.64 (24.55)	24.26 (25.92)	21.96 (25.76)	19.83 (25.99)
0.95	2.34 (2.33)	8.49 (8.56)	16.37 (16.82)	20.90 (22.05)	24.29 (25.20)	26.79 (26.26)	30.81 (30.68)	34.79 (40.10)
				$\Delta\nu/\nu$				
−0.80	13.99 (14.95)	8.43 (7.59)	17.36 (17.43)	30.87 (26.84)	34.16 (29.24)	39.47 (32.44)	36.78 (28.54)	27.04 (25.92)
−0.50	12.33 (12.60)	8.02 (7.42)	9.50 (10.35)	11.41 (15.06)	15.56 (18.93)	17.12 (22.32)	9.05 (24.82)	4.48 (24.23)
0.00	8.87 (8.50)	9.14 (8.04)	11.67 (11.21)	12.77 (13.82)	13.59 (14.68)	14.86 (17.10)	12.12 (17.61)	7.49 (17.78)
0.50	10.59 (10.10)	10.28 (9.98)	14.09 (12.99)	16.75 (16.13)	18.04 (17.57)	17.50 (17.58)	15.28 (17.45)	13.99 (17.17)
0.80	12.37 (11.36)	12.23 (11.90)	15.76 (15.13)	18.34 (17.92)	20.63 (21.55)	22.24 (23.61)	22.50 (26.68)	19.50 (27.49)
0.95	13.13 (12.36)	12.22 (11.84)	17.53 (18.10)	21.45 (21.85)	24.48 (25.48)	28.69 (28.25)	35.40 (35.79)	41.52 (49.53)
				$\Delta d_L/d_L$				
−0.80	109.24 (48.12)	124.30 (51.67)	114.53 (51.11)	114.46 (63.14)	125.25 (66.61)	127.59 (71.34)	121.86 (66.87)	117.86 (68.45)
−0.50	103.65 (48.38)	129.83 (54.84)	131.48 (51.71)	130.28 (52.81)	135.20 (54.66)	136.64 (55.23)	124.22 (56.76)	109.45 (57.42)
0.00	99.20 (49.37)	113.16 (50.23)	114.13 (48.00)	112.25 (47.21)	108.44 (45.96)	110.75 (47.10)	107.76 (46.74)	97.85 (47.04)
0.50	103.31 (48.77)	110.10 (49.15)	110.33 (47.05)	106.26 (45.79)	104.54 (46.31)	104.99 (44.27)	102.17 (45.73)	97.40 (44.49)
0.80	103.08 (49.66)	105.15 (47.99)	103.31 (44.34)	100.17 (42.86)	104.40 (42.41)	101.70 (42.34)	103.96 (42.39)	100.91 (42.72)
0.95	102.05 (47.09)	99.08 (44.33)	88.38 (36.40)	85.40 (36.85)	88.10 (39.02)	88.58 (39.61)	88.39 (42.79)	91.10 (51.23)
				$\Delta m_1^s/m_1^s$				
−0.80	40.98 (45.62)	31.75 (30.72)	35.04 (39.82)	39.54 (50.16)	42.04 (54.91)	49.19 (60.53)	48.16 (59.19)	38.07 (58.29)
−0.50	37.89 (41.78)	29.41 (30.81)	30.78 (33.11)	31.96 (38.60)	35.49 (45.52)	36.42 (49.73)	33.02 (53.81)	28.95 (55.42)
0.00	30.70 (32.47)	29.80 (30.15)	30.29 (32.31)	31.57 (35.59)	31.46 (37.38)	31.79 (40.52)	28.29 (43.06)	23.98 (44.56)
0.50	34.68 (36.27)	32.27 (34.38)	33.18 (36.65)	34.18 (38.88)	34.82 (41.31)	35.44 (42.05)	33.88 (43.33)	28.58 (43.98)
0.80	37.22 (38.46)	34.15 (37.63)	34.39 (39.69)	34.34 (42.72)	36.02 (47.98)	37.41 (51.04)	38.86 (57.85)	37.79 (61.08)
0.95	37.64 (39.72)	33.05 (36.85)	32.69 (43.14)	35.02 (46.72)	37.59 (52.18)	40.99 (58.19)	48.21 (71.12)	54.54 (92.24)
				$\Delta m_2^s/m_2^s$				
−0.80	37.94 (41.76)	37.66 (39.26)	52.09 (56.24)	63.16 (66.60)	66.53 (68.92)	72.07 (71.17)	74.50 (66.15)	69.50 (62.66)
−0.50	33.88 (37.77)	40.83 (42.93)	45.74 (48.60)	49.70 (55.92)	56.81 (60.14)	59.23 (62.33)	49.08 (62.41)	36.17 (59.93)
0.00	29.69 (34.13)	38.23 (40.26)	45.75 (48.84)	47.74 (51.72)	50.02 (52.34)	53.09 (54.47)	50.45 (53.06)	43.21 (51.57)
0.50	32.82 (36.51)	37.25 (41.91)	45.75 (49.90)	50.89 (55.81)	52.98 (57.25)	53.51 (55.19)	51.94 (53.01)	50.32 (51.12)
0.80	35.37 (38.93)	38.37 (44.42)	45.55 (51.92)	50.55 (56.62)	55.09 (60.72)	57.34 (61.86)	59.69 (63.35)	58.78 (62.21)
0.95	34.17 (37.98)	35.93 (42.42)	41.92 (48.82)	48.28 (54.91)	54.21 (61.09)	58.86 (64.34)	65.04 (69.39)	70.40 (80.83)
				$\Delta M_{tot}^s/M_{tot}^s$				
−0.80	12.96 (12.72)	19.25 (16.84)	21.39 (17.91)	22.59 (19.26)	24.02 (19.86)	24.56 (19.20)	26.05 (18.56)	25.47(18.92)
−0.50	12.53 (12.35)	20.71 (19.89)	23.45 (20.43)	24.91 (20.24)	26.94 (20.46)	27.89 (19.28)	28.43 (18.05)	25.42 (18.20)
0.00	11.54 (11.66)	19.06 (17.57)	22.15 (19.70)	22.99 (19.14)	24.28 (18.83)	24.71 (17.86)	24.89 (17.10)	23.40 (16.57)
0.50	13.03 (12.68)	18.43 (17.24)	21.77 (19.41)	23.44 (19.16)	24.66 (19.09)	26.28 (17.62)	26.56 (17.07)	25.75 (16.66)
0.80	13.57 (13.25)	18.27 (17.51)	21.49 (18.76)	23.30 (19.23)	25.58 (19.08)	26.69 (17.83)	29.45 (17.68)	30.97 (17.81)
0.95	13.72 (13.18)	17.70 (16.37)	18.37 (15.27)	19.96 (15.18)	22.76 (16.32)	23.48 (16.41)	25.38 (18.74)	27.09 (24.16)
				$\Delta\chi_1/\chi_1$				
−0.80	57.79 (59.56)	62.54 (68.11)	69.60 (84.77)	113.42 (119.57)	125.66 (125.30)	134.07 (124.58)	142.31 (131.19)	145.65 (134.80)
−0.50	167.26 (167.97)	190.27 (193.72)	191.59 (192.84)	200.30 (202.10)	203.99 (203.28)	212.54 (207.80)	206.81 (211.35)	199.01 (222.16)
0.50	142.76 (146.91)	161.14 (165.53)	155.77 (170.61)	164.73 (171.53)	171.11 (176.87)	176.26 (180.27)	188.26 (198.70)	187.56 (201.88)
0.80	38.25 (38.19)	48.82 (50.35)	53.32 (54.15)	54.50 (54.87)	57.82 (55.19)	59.03 (57.63)	65.26 (65.47)	71.83 (70.79)
0.95	10.42 (10.35)	17.02 (17.86)	20.70 (21.17)	21.32 (22.72)	21.71 (23.13)	21.20 (22.56)	19.83 (23.97)	20.31 (27.11)
				$\Delta\chi_2/\chi_2$				
−0.80	100.77 (114.01)	79.72 (83.05)	117.00 (118.74)	143.12 (145.64)	150.22 (156.60)	163.02 (158.71)	167.28 (161.52)	156.74 (166.48)
−0.50	207.89 (208.63)	203.40 (200.99)	212.48 (213.34)	220.37 (227.68)	242.12 (244.35)	248.53 (252.90)	255.91 (260.95)	249.87 (258.30)
0.50	207.34 (208.59)	222.72 (218.71)	225.93 (225.32)	229.50 (225.50)	234.26 (224.77)	232.81 (231.76)	230.68 (237.31)	234.28 (237.26)
0.80	98.71 (90.01)	118.82 (117.89)	135.50 (131.24)	138.07 (136.65)	138.26 (149.40)	140.59 (137.77)	129.21 (146.30)	131.95 (143.18)
0.95	42.45 (40.38)	68.89 (67.14)	108.41 (112.57)	123.05 (124.62)	120.47 (132.93)	126.90 (127.62)	131.70 (136.27)	134.21 (136.63)

Note. For all runs, $q = 1.25$, $\iota = \pi/3$, and S/N = 20. The spin column represents the equal component spins (i.e., $\chi_1 = \chi_2$) along the orbital angular momentum $\boldsymbol{L}$. The results in parenthesis denote the corresponding face-on case (i.e., $\iota = 0$).

modes reach the most sensitive frequency range of the detector. The $\chi_1 = \chi_2 = 0.95$ systems, in particular, behave somewhat unexpectedly above $M_{tot} \gtrsim 450\ M_\odot$. We find that these systems have a bimodal distribution in the parameters M_c, ν, $m_{1,2}$, and χ_2, which causes the width of the posteriors to increase

significantly. We shall discuss these features in more detail in Section 3.3 below.

Figure 4 shows the posterior relative widths for the parameters when the mass ratio of the binaries is $q = 1.25$. As with the $q = 4$ binaries, there is a trend for each spin, with a few exceptions. First,

Table 2
The 95% Width (as a Percentage) of One-dimensional Marginalized Posteriors Scaled by the True Value for Injections and Recoveries with SEOBNRHM Waveforms

Spin	$M_{tot} = 50\ M_\odot$	$100\ M_\odot$	$150\ M_\odot$	$200\ M_\odot$	$250\ M_\odot$	$300\ M_\odot$	$400\ M_\odot$	$500\ M_\odot$
				$\Delta M_c/M_c$				
−0.80	3.06 (5.10)	24.23 (64.35)	38.81 (62.92)	47.22 (68.48)	60.64 (84.09)	63.12 (74.90)	57.12 (73.01)	51.07 (72.81)
−0.50	2.44 (4.06)	35.08 (50.82)	55.56 (62.38)	61.89 (58.60)	62.30 (74.33)	59.85 (64.66)	56.14 (74.01)	48.41 (60.82)
0.00	1.81 (2.93)	11.28 (18.71)	33.00 (73.94)	48.90 (59.53)	51.53 (42.28)	55.06 (47.46)	49.16 (45.79)	40.34 (45.50)
0.50	1.44 (2.22)	7.91 (11.24)	18.25 (27.65)	27.16 (46.72)	31.72 (80.82)	33.31 (73.86)	31.89 (41.36)	29.96 (36.71)
0.80	1.25 (1.82)	5.32 (7.62)	11.20 (17.35)	17.42 (27.00)	21.86 (35.60)	25.20 (45.22)	27.15 (75.79)	25.94 (54.37)
0.95	1.17 (1.36)	4.06 (5.82)	8.83 (12.06)	12.99 (16.91)	15.84 (20.42)	17.84 (23.91)	19.32 (34.02)	23.16 (42.01)
				$\Delta\nu/\nu$				
−0.80	25.59 (28.17)	29.72 (57.01)	41.66 (51.78)	51.33 (55.62)	57.07 (73.90)	58.96 (65.28)	53.84 (65.64)	49.11 (67.59)
−0.50	25.95 (34.98)	40.70 (56.41)	47.91 (48.07)	52.23 (45.70)	57.14 (66.92)	56.23 (55.03)	53.97 (68.97)	47.95 (57.68)
0.00	23.03 (36.59)	25.14 (33.43)	34.70 (64.77)	45.75 (49.93)	48.53 (32.46)	49.03 (39.06)	48.30 (39.64)	42.00 (38.73)
0.50	25.20 (35.75)	21.09 (24.83)	21.08 (27.57)	24.84 (41.79)	29.09 (80.86)	33.28 (72.85)	35.44 (35.61)	35.33 (31.75)
0.80	18.84 (24.80)	16.15 (18.05)	14.86 (18.50)	16.11 (22.68)	18.42 (31.15)	21.69 (43.34)	25.10 (90.22)	25.53 (67.91)
0.95	15.18 (16.45)	11.74 (13.57)	13.71 (15.90)	16.10 (18.48)	18.62 (21.99)	19.80 (25.81)	20.08 (40.85)	30.16 (54.17)
				$\Delta d_L/d_L$				
−0.80	80.23 (26.19)	79.94 (113.39)	85.19 (118.92)	88.45 (132.54)	151.00 (163.15)	144.86 (151.74)	118.05 (158.19)	103.42 (180.17)
−0.50	87.40 (25.58)	123.58 (90.76)	150.47 (119.08)	152.48 (114.32)	144.31 (142.43)	132.20 (126.29)	117.51 (146.26)	102.48 (143.31)
0.00	85.53 (25.60)	81.41 (42.10)	96.18 (128.58)	107.68 (107.21)	103.42 (91.97)	106.08 (92.65)	93.52 (92.39)	80.20 (98.80)
0.50	88.50 (25.37)	80.90 (31.63)	77.94 (50.67)	79.40 (74.99)	78.03 (121.11)	75.25 (115.71)	71.23 (81.83)	64.99 (76.73)
0.80	86.90 (24.40)	80.97 (26.64)	75.31 (35.61)	73.42 (46.28)	71.99 (56.41)	70.28 (67.01)	68.52 (108.58)	66.31 (86.28)
0.95	91.11 (24.53)	81.52 (24.88)	73.04 (28.32)	66.87 (32.59)	62.08 (35.68)	59.68 (38.67)	55.85 (49.72)	53.80 (58.03)
				$\Delta m_1^s/m_1^s$				
−0.80	28.61 (30.60)	18.60 (35.26)	17.46 (37.51)	18.79 (39.56)	23.28 (48.99)	27.40 (47.92)	26.40 (48.43)	25.64 (47.64)
−0.50	24.55 (34.49)	24.39 (32.05)	25.06 (35.54)	24.97 (36.08)	25.56 (45.59)	25.68 (41.53)	25.83 (48.42)	25.85 (46.06)
0.00	20.64 (33.46)	19.94 (25.12)	19.14 (41.07)	20.05 (37.02)	19.59 (30.61)	18.69 (34.05)	18.43 (35.20)	16.94 (34.39)
0.50	23.68 (33.91)	21.06 (23.13)	19.97 (20.39)	20.07 (21.57)	20.00 (48.40)	20.48 (48.48)	20.80 (32.73)	18.87 (30.40)
0.80	18.45 (24.90)	18.34 (18.24)	18.01 (17.19)	17.80 (16.71)	17.97 (17.91)	18.26 (22.75)	18.79 (60.33)	18.89 (50.79)
0.95	16.46 (17.03)	15.82 (14.01)	16.84 (14.48)	16.90 (15.31)	17.05 (16.40)	17.10 (18.18)	16.96 (27.45)	17.88 (37.37)
				$\Delta m_2^s/m_2^s$				
−0.80	18.69 (20.44)	45.03 (146.80)	69.64 (153.41)	81.87 (150.82)	83.61 (169.60)	79.82 (154.00)	70.84 (155.98)	65.17 (158.58)
−0.50	20.53 (25.88)	59.73 (99.74)	91.40 (153.57)	96.89 (143.49)	97.26 (165.00)	91.11 (145.36)	84.40 (159.96)	72.80 (145.10)
0.00	19.50 (28.76)	28.04 (35.48)	52.90 (169.22)	76.55 (155.11)	80.97 (124.01)	81.61 (129.71)	76.62 (124.83)	64.40 (122.44)
0.50	20.67 (27.67)	22.16 (21.72)	28.85 (33.26)	38.10 (55.15)	45.59 (165.68)	51.95 (168.77)	55.17 (116.65)	55.18 (109.47)
0.80	16.46 (18.60)	19.14 (15.52)	21.64 (20.14)	25.62 (28.14)	29.83 (38.69)	34.78 (53.36)	40.35 (167.81)	39.92 (146.18)
0.95	16.01 (12.87)	18.15 (12.95)	23.36 (17.06)	27.19 (20.32)	30.24 (24.29)	31.58 (27.97)	32.24 (42.50)	39.73 (55.75)
				$\Delta M_{tot}^s/M_{tot}^s$				
−0.80	19.86 (20.83)	15.32 (18.74)	17.34 (18.87)	18.85 (19.11)	19.63 (19.91)	19.72 (19.39)	18.53 (19.57)	18.23 (19.92)
−0.50	16.36 (22.69)	16.73 (16.98)	21.36 (20.11)	21.45 (19.54)	21.09 (19.25)	20.73 (18.17)	20.92 (18.55)	21.39 (18.63)
0.00	13.90 (21.34)	14.07 (15.35)	15.61 (17.69)	17.98 (18.57)	18.08 (18.44)	17.90 (16.97)	16.82 (16.23)	14.80 (16.03)
0.50	16.09 (21.84)	16.26 (15.65)	17.38 (14.79)	19.10 (14.29)	19.81 (15.09)	20.16 (16.45)	19.97 (15.94)	18.11 (15.28)
0.80	13.25 (16.61)	15.32 (12.96)	16.36 (12.98)	17.08 (13.02)	17.66 (12.65)	18.30 (12.67)	18.84 (21.24)	18.74 (18.72)
0.95	13.21 (11.76)	14.63 (10.25)	16.24 (10.73)	16.89 (11.19)	17.27 (11.41)	17.40 (11.86)	16.95 (15.60)	16.54 (20.55)
				$\Delta\chi_1/\chi_1$				
−0.80	68.73 (57.12)	50.48 (89.33)	49.23 (101.19)	54.29 (114.19)	115.62 (119.20)	119.17 (120.38)	112.42 (125.58)	109.84 (127.39)
−0.50	100.66 (115.24)	122.17 (140.52)	151.05 (184.85)	164.38 (190.73)	158.42 (196.81)	150.45 (196.82)	148.16 (206.80)	151.68 (208.22)
0.50	46.73 (48.52)	46.42 (51.89)	58.35 (68.90)	67.49 (81.77)	69.50 (102.69)	69.81 (168.79)	71.77 (197.82)	69.04 (211.44)
0.80	14.41 (15.49)	14.98 (17.20)	17.47 (23.66)	22.27 (29.43)	25.49 (31.29)	26.77 (30.52)	26.04 (40.26)	23.95 (62.71)
0.95	4.36 (4.54)	4.40 (5.49)	4.95 (7.04)	5.51 (8.29)	6.14 (8.50)	6.54 (8.38)	6.91 (8.43)	7.15 (8.11)
				$\Delta\chi_2/\chi_2$				
−0.80	159.54 (162.59)	152.68 (146.97)	148.79 (149.74)	156.49 (161.73)	165.62 (168.52)	171.08 (169.93)	171.03 (169.06)	170.25 (174.42)
−0.50	262.59 (270.20)	256.04 (258.78)	245.29 (243.53)	257.00 (252.92)	264.46 (260.38)	273.12 (271.42)	271.56 (266.43)	271.45 (268.27)
0.50	266.38 (257.87)	259.36 (265.83)	256.61 (268.90)	255.57 (273.41)	245.65 (277.63)	250.18 (239.98)	244.83 (248.33)	238.23 (252.89)
0.80	143.92 (149.29)	148.14 (157.34)	152.42 (165.12)	153.04 (170.84)	151.81 (170.30)	149.25 (172.16)	145.39 (173.50)	142.27 (152.74)
0.95	67.77 (73.63)	83.15 (97.37)	103.08 (124.20)	114.54 (139.45)	121.39 (144.29)	117.70 (143.50)	109.63 (147.88)	115.18 (145.90)

Note. For all runs, $q = 4$, $\iota = \pi/3$, and S/N = 20. The spin column represents the equal component spins (i.e., $\chi_1 = \chi_2$) along the orbital angular momentum $\boldsymbol{L}$. The results in parenthesis denote the corresponding face-on case (i.e., $\iota = 0$).

we find that systems with $\chi_1 = \chi_2 = 0.95$ show bimodality even when the total mass is as low as 200 $M_\odot$, and continue doing so for higher total masses. The bimodality in χ_2 appears throughout (i.e., even when the total mass is $\sim$100 $M_\odot$). Second, some systems show an unusual trend with total mass (e.g., see the plot of total mass uncertainty in Figure 4). The uncertainty increases

again after 350 $M_\odot$, where we would expect it to decrease. We find that for such parameter choices, there is a strong correlation between the total mass M_{tot} and the primary spin χ_1. Additionally, the posterior for χ_1 also develops a mild bimodality.

As stressed before, we are mostly interested in characterizing the uncertainty in the measurements of source-frame masses,

Table 3
The 95% Width (as a Percentage) of One-dimensional Marginalized Posteriors Scaled by the True Value for Injections and Recoveries with SEOBNRHM Waveforms

Spin	$M_{tot} = 50\,M_\odot$	$100\,M_\odot$	$150\,M_\odot$	$200\,M_\odot$	$250\,M_\odot$	$300\,M_\odot$	$400\,M_\odot$	$500\,M_\odot$
				$\Delta M_c/M_c$				
−0.80	1.83 (3.14)	12.19 (72.67)	83.57 (130.25)	219.60 (147.28)	123.69 (136.57)	50.09 (137.15)	30.90 (152.80)	26.94 (117.98)
−0.50	2.48 (2.79)	10.31 (30.93)	49.03 (163.31)	65.12 (122.41)	68.00 (127.08)	66.58 (126.37)	55.53 (134.03)	48.18 (105.43)
0.00	1.49 (1.95)	4.72 (12.00)	13.82 (54.59)	25.68 (129.93)	36.25 (92.34)	38.47 (87.81)	35.76 (92.42)	31.84 (72.31)
0.50	1.22 (1.64)	3.08 (5.80)	7.63 (18.03)	14.83 (42.78)	21.30 (82.63)	26.75 (148.46)	25.19 (64.02)	22.69 (62.52)
0.80	0.99 (1.36)	2.36 (4.26)	4.92 (10.41)	8.16 (17.92)	11.66 (26.27)	16.05 (40.96)	22.34 (116.26)	27.49 (136.58)
0.95	0.64 (0.81)	1.68 (3.20)	3.05 (6.38)	4.31 (9.82)	5.28 (12.81)	6.26 (17.34)	7.83 (36.98)	9.82 (62.95)
				$\Delta\nu/\nu$				
−0.80	28.31 (36.62)	25.15 (103.99)	95.19 (136.93)	198.58 (160.93)	120.07 (148.38)	61.28 (147.45)	37.00 (174.71)	32.79 (143.79)
−0.50	53.84 (50.44)	36.63 (55.97)	59.75 (177.13)	73.93 (131.25)	78.65 (136.07)	77.11 (135.84)	67.40 (148.57)	60.67 (126.30)
0.00	41.79 (49.66)	24.27 (36.95)	26.34 (72.55)	35.73 (136.06)	47.88 (94.84)	51.30 (91.34)	50.82 (100.71)	51.37 (73.80)
0.50	41.66 (72.24)	24.14 (35.21)	18.86 (31.66)	20.92 (49.91)	24.17 (94.04)	28.02 (188.81)	26.42 (59.79)	25.21 (58.16)
0.80	32.96 (47.31)	18.67 (26.10)	14.35 (20.61)	13.06 (22.18)	13.93 (27.57)	16.08 (43.81)	20.59 (160.46)	25.10 (205.87)
0.95	14.88 (16.97)	10.56 (13.90)	9.65 (12.63)	9.70 (14.14)	9.57 (16.04)	9.91 (20.75)	10.24 (47.39)	11.32 (87.60)
				$\Delta d_L/d_L$				
−0.80	73.11 (25.06)	65.60 (154.89)	231.74 (311.80)	779.20 (361.17)	396.09 (359.12)	107.18 (374.55)	54.23 (448.51)	36.62 (443.06)
−0.50	72.74 (25.24)	66.74 (65.21)	104.59 (373.35)	123.77 (306.22)	125.95 (326.62)	124.00 (329.27)	103.44 (383.32)	93.69 (363.36)
0.00	74.63 (24.48)	63.99 (34.19)	59.96 (103.53)	66.07 (286.97)	75.47 (224.17)	74.46 (215.62)	68.73 (240.12)	60.79 (224.08)
0.50	78.26 (24.18)	68.11 (26.58)	62.94 (40.44)	62.63 (76.50)	62.80 (139.50)	64.71 (270.90)	57.53 (163.59)	54.76 (160.13)
0.80	76.81 (23.87)	69.44 (24.91)	64.64 (29.68)	62.21 (38.27)	58.95 (47.82)	59.18 (66.28)	58.95 (188.20)	63.14 (243.47)
0.95	76.34 (21.90)	69.09 (24.14)	64.40 (24.37)	59.30 (27.87)	56.62 (30.44)	52.64 (33.92)	48.95 (58.46)	49.68 (96.24)
				$\Delta m_1^s/m_1^s$				
−0.80	24.98 (34.85)	13.70 (26.92)	13.84 (34.98)	34.42 (39.55)	14.71 (40.06)	9.44 (40.44)	5.93 (47.07)	4.87 (43.39)
−0.50	47.98 (41.47)	25.17 (24.95)	20.87 (43.39)	19.63 (37.73)	18.56 (38.88)	17.75 (39.69)	17.34 (42.20)	17.63 (39.50)
0.00	29.90 (35.83)	17.34 (22.64)	13.98 (21.61)	12.42 (38.02)	12.10 (32.02)	11.74 (31.30)	11.83 (33.34)	12.78 (28.82)
0.50	28.84 (44.84)	18.27 (26.33)	14.86 (21.08)	13.98 (18.85)	13.02 (21.13)	12.80 (49.78)	11.73 (23.69)	11.33 (23.00)
0.80	24.22 (31.94)	15.52 (21.40)	13.52 (17.59)	12.97 (16.11)	12.57 (14.71)	12.73 (14.82)	11.96 (39.63)	11.48 (58.17)
0.95	12.57 (13.74)	11.36 (12.32)	11.96 (11.08)	12.39 (11.18)	12.77 (10.91)	12.55 (11.05)	12.80 (18.07)	13.71 (31.41)
				$\Delta m_2^s/m_2^s$				
−0.80	14.96 (18.74)	22.50 (123.95)	130.83 (346.02)	403.11 (353.57)	166.47 (323.09)	75.83 (311.73)	45.95 (359.18)	41.34 (330.96)
−0.50	27.13 (24.63)	23.81 (51.06)	73.94 (421.33)	98.56 (336.48)	101.92 (328.70)	98.20 (318.44)	80.91 (338.26)	69.20 (322.25)
0.00	20.90 (23.89)	15.61 (24.89)	24.92 (78.17)	40.38 (367.98)	55.33 (293.82)	58.81 (277.45)	56.95 (283.17)	54.70 (249.85)
0.50	21.44 (34.68)	14.79 (17.94)	15.59 (24.15)	22.33 (51.83)	29.00 (105.19)	35.61 (363.76)	33.97 (217.18)	31.52 (210.56)
0.80	18.00 (23.10)	13.30 (12.75)	13.55 (13.28)	15.24 (19.26)	17.35 (27.98)	21.03 (46.00)	26.23 (173.56)	30.84 (347.95)
0.95	10.50 (9.01)	11.94 (8.56)	13.74 (9.74)	15.11 (12.40)	16.27 (15.10)	16.88 (19.80)	17.79 (43.84)	19.40 (77.47)
				$\Delta M_{tot}^s/M_{tot}^s$				
−0.80	21.50 (30.09)	11.63 (19.21)	12.20 (19.37)	15.49 (18.28)	11.32 (18.91)	10.10 (18.95)	7.65 (20.27)	7.20 (20.36)
−0.50	41.23 (35.53)	21.40 (20.46)	19.88 (19.78)	20.04 (19.07)	18.74 (18.07)	17.64 (17.82)	15.60 (18.67)	15.06 (18.98)
0.00	25.48 (30.52)	14.95 (18.87)	12.22 (16.48)	11.54 (18.14)	11.09 (17.21)	10.44 (16.04)	9.66 (16.23)	9.58 (15.87)
0.50	24.46 (37.56)	15.99 (22.54)	13.41 (18.22)	13.03 (16.10)	12.67 (14.84)	12.97 (18.99)	11.90 (14.01)	11.40 (14.05)
0.80	20.81 (27.06)	13.89 (18.54)	12.56 (15.57)	12.42 (14.39)	12.23 (13.27)	12.53 (12.34)	11.98 (21.73)	11.60 (27.24)
0.95	11.20 (11.86)	10.79 (10.84)	11.68 (9.89)	12.21 (10.13)	12.73 (9.80)	12.58 (9.62)	12.91 (13.58)	13.74 (22.32)
				$\Delta\chi_1/\chi_1$				
−0.80	53.72 (68.55)	33.18 (64.17)	51.25 (97.30)	125.65 (110.64)	96.31 (114.81)	54.26 (116.72)	33.30 (118.64)	28.77 (116.68)
−0.50	137.67 (126.95)	81.82 (87.06)	105.28 (167.70)	112.60 (186.32)	117.31 (187.19)	123.53 (192.92)	137.55 (194.92)	140.38 (197.06)
0.50	36.01 (54.61)	25.42 (33.53)	25.75 (39.63)	32.19 (54.47)	37.47 (64.16)	41.37 (124.42)	36.68 (206.31)	38.38 (216.32)
0.80	7.57 (7.38)	7.90 (11.10)	8.45 (14.28)	9.75 (17.74)	11.05 (19.76)	13.72 (20.67)	16.18 (22.60)	18.33 (49.87)
0.95	2.39 (3.19)	2.09 (3.95)	1.95 (4.50)	1.82 (5.46)	1.74 (5.25)	1.72 (5.00)	1.71 (5.34)	1.88 (5.57)
				$\Delta\chi_2/\chi_2$				
−0.80	170.25 (172.21)	170.05 (170.02)	171.44 (161.66)	170.63 (167.33)	170.89 (173.95)	174.03 (173.59)	169.61 (173.30)	169.13 (173.63)
−0.50	271.18 (276.01)	272.48 (277.39)	275.31 (260.76)	270.29 (269.17)	273.27 (271.54)	276.18 (272.73)	277.80 (275.65)	278.82 (271.75)
0.50	281.33 (264.94)	268.18 (274.95)	261.38 (270.31)	252.48 (273.60)	245.65 (274.66)	246.45 (266.32)	250.92 (253.02)	269.66 (256.35)
0.80	151.86 (124.07)	143.18 (164.41)	140.32 (163.40)	142.57 (166.37)	141.21 (168.46)	145.89 (170.90)	144.07 (177.06)	148.05 (161.97)
0.95	86.72 (104.97)	82.09 (103.09)	96.21 (117.98)	100.94 (136.49)	104.87 (144.37)	106.65 (143.13)	105.35 (146.09)	108.04 (146.61)

Note. For all runs, $q = 10$, $\iota = \pi/3$, and S/N = 20. The spin column represents the equal component spins (i.e., $\chi_1 = \chi_2$) along the orbital angular momentum $\boldsymbol{L}$. The results in parenthesis denote the corresponding face-on case (i.e., $\iota = 0$).

because they could help us to understand the precision with which, e.g., the mass function of IMBHs can be constructed from GW measurements in upcoming observations, and also to determine the probability that the observed BH's mass is in the mass gap. This information can be extracted from Figures 5 and 6. The primary mass for all the systems with $q = 4$ can be measured with an uncertainty of ~17%–25%[12] while for binaries with $q = 1.25$ the uncertainties are ~30%–40% except when $\chi_1 = \chi_2 > 0.8$, where bimodality further worsens the precision, pushing the uncertainties to ~60%.

_____
[12] Including the $\chi_1 = \chi_2 = -0.8$ results from Table 2.

The improvement in the precision for $q = 4$ binaries is due to the presence of higher modes in the gravitational signal, which break the degeneracy among parameters and lead to a better measurement of m_1 and d_L. For high mass ratio ($q = 10$), the precision improves further, bringing the uncertainties down to $\sim$11%–20% (see Table 3) except when $M_{\rm tot} < 100\ M_\odot$, where we see a very strong correlation among the parameters $M_{\rm tot}$, m_1, m_2, and q. This is also true for even smaller mass ratios. We can see this from Figure 3 for $q = 4$, where, contrary to our expectation, the precision of the total-mass measurement at $50\ M_\odot$ is poorer than that at $100\ M_\odot$. We observe a similar trend in the measurement of the primary mass m_1. The secondary mass, on the other hand, is measured with relatively poor precision: for symmetric systems ($q \sim 1$), the uncertainties lie between 30% and 60% except for binaries with $\chi_1 = \chi_2 \geqslant 0.8$, for which the uncertainty can reach 80%. For higher mass-ratio signals, the uncertainty can exceed 100%, except for a few highly spinning aligned systems (e.g., $\chi_1 = \chi_2 \geqslant 0.5$) where the uncertainty can reduce to $\sim$10%–30% (see Table 3). The total source mass ($M_{\rm tot}^s$), however, is measured with a much better precision, with uncertainties in the range $\sim$10%–30%, regardless of the details of the signals.

From Figures 3 and 4, we also see that component spins can only be measured poorly. The primary spin (χ_1) can be measured better than $\sim$50% only for asymmetric binaries that have high component spins, $\chi_1 = \chi_2 > 0.5$. Figure 4 shows that for nearly symmetric systems, unless the spins are $\chi_1 = \chi_2 > 0.8$, we might not be able to measure the primary component spin better than 50%. But, as expected, for very high mass-ratio signals, we can measure the primary spin with an uncertainty lower than $\sim$30% if the systems are aligned (see Table 3). Measuring the secondary spin, however, seems to be difficult for almost all of the IMBH binaries.

To understand how much the neglect of spin precession in our waveform model affects these precisions, we simulate a few moderately spinning, precessing GW signals with the `NRSurPHM` waveform model (Varma et al. 2019b), and analyze them with the spinning, nonprecessing `SEOBNRPHM` model. Mild spin precession is motivated from the LIGO–Virgo observations (Abbott et al. 2019a, 2020c) so far. More specifically, we fix the angle between the primary spin χ_1 and the total angular momentum J (i.e., the tilt angle) to be 30° except for antialigned binaries, for which the tilt angle is taken to be 210°, while the magnitudes of the component spin vectors are taken to be the same as their nonprecessing counterparts. The other angles required to define the components of the spins on the orbital plane are taken to be zero. All of these quantities are defined at a reference frequency, which we choose to be $f_{\rm ref} = 11$ Hz. These results are indicated by the small dots in Figures 5 and 6. We can see that the uncertainties in the component-mass measurement change only by $\lesssim$5%. The additional systematic bias introduced by the neglect of precession in the recovery model is also $\lesssim$5%. Thus, a mild precession in the signals is not expected to change the results established here significantly, as long as they are recovered with spinning, nonprecessing waveforms. We plan in the future to carry out a comprehensive study that will analyze spinning, precessing GW signals with precessing waveforms.

We also produced results with the noise spectral density projected for the O5 run (Abbott et al. 2020a), but at the same $S/N = 20$, since a priori we do not know what the distribution of the observed S/Ns is going to be. However, we do expect that a larger number of IMBHBs should be observed at a given S/N during O5 than during O4, as also shown in Section 1. We find that, at O5 sensitivity and $S/N = 20$, the precision of detector-frame masses improves only by a few percent (e.g., for the chirp mass M_c it improves by $\sim$6%), while for the source-frame component masses, which we are mainly interested in, it remains mostly unchanged.

When considering also the results in Tables 1, 2, and 3, obtained at inclination angle $\pi/3$ and mass ratio $q = 10$, and at zero inclination angle for mass ratios $q = 1$, 4, and 10, we can summarize the main findings as follows. At inclination $\pi/3$, for quite asymmetric IMBHB systems (i.e., $q \sim 10$), we could measure the primary mass with uncertainties 11%–25%, whereas for symmetric binaries ($q \sim 1$), the uncertainties are expected to be $\sim$30%–40% except for systems with component spins $\chi_1 = \chi_2 \gtrsim 0.8$, where the uncertainties can reach $\sim$60% due to the presence of bimodality. At zero inclination, however, the uncertainty in the primary mass can also go up to $\sim$60% independently of the mass ratio (except for $\chi_{1,2} \gtrsim 0.80$ systems, where the precision becomes even worse due to bimodality). However, for the bulk of the parameter space, even at zero inclination, the uncertainty is $\lesssim$40% for the primary mass, where this upper limit is set by the high-mass IMBHBs (e.g., $M_{\rm tot} \sim 500\ M_\odot$). An important question in astrophysics concerns the nature of the IMBH mass function. Although upcoming LIGO and Virgo observations may not be capable of observing enough IMBHs to reconstruct their mass function, they hold the potential to provide us with much better mass measurements than what might be possible with electromagnetic observations. In Section 4.6, we shall study in more detail the implications of the component-mass measurements in assessing the BH upper stellar-mass gap.

From Figures 3 and 4, we can see that measuring the luminosity distance (d_L) with precision better than 50% may not be possible at high inclination ($\iota = \pi/3$). On the other hand, Table 1 shows that symmetric face-on IMBH binaries, which emit GW signals with the highest amplitudes, can allow us to constrain d_L with uncertainty $<$50%. When the total mass and spins are high (e.g., $M_{\rm tot} \gtrsim 400\ M_\odot$, $\chi_1 = \chi_2 \gtrsim 0.5$), we can even constrain the luminosity distance with uncertainties less than 40% (20%) at O4 (O5) sensitivity. Given the large detection horizon distance for IMBH binaries, these luminosity distance measurements could be valuable for statistical constraints on cosmological parameters (Schutz 1986; Abbott et al. 2021a), but this will depend on the rate of observed events.

3.3. Bimodality in Component Masses and Spins

As we discussed in the previous section, for sufficiently high total masses, highly spinning IMBHB systems (i.e., $\chi_1 = \chi_2 \gtrsim 0.8$) can exhibit bimodality in the posterior distributions of some parameters. As an example, we show in Figure 7 the results obtained for an IMBHB system with $M_{\rm tot} = 500\ M_\odot$, $q = 1.25$, $\chi_1 = \chi_2 = 0.95$, and $\iota = \pi/3$ at $S/N = 20$. To better understand the bimodality we inject and run the Bayesian analysis with two spinning, nonprecessing waveform models: `SEOBNRHM` and `PhenomHM` (García-Quirós et al. 2020). For both models we observe bimodal posterior distributions in the component masses $m_{1,2}^s$, the secondary component spin χ_2, and the inclination angle ι.

To understand the results, we compare in the (left) right panel of Figure 8 the (whitened) waveforms for the `SEOBNRHM`
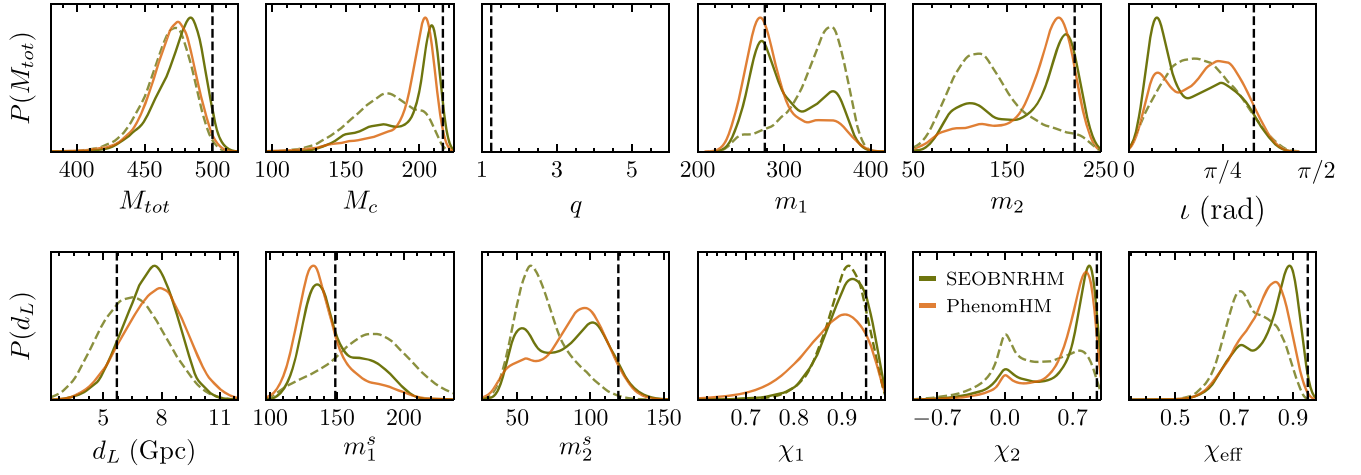
Figure 7. Posterior distributions of the parameters for an injected signal with $M_{\rm tot} = 500\,M_\odot$, $q = 1.25$, $\chi_1 = \chi_2 = 0.95$, and $\iota = \pi/3$ at S/N = 20. The dashed lines show the posteriors when the SEOBNRHM injected signal is recovered with 22 mode waveform model SEOBNR. In each panel the vertical dashed lines indicate the true (injected) value of the parameter. Both SEOBNRHM and PhenomHM models show bimodality in various parameters (e.g., the component masses $m_{1,2}$). The SEOBNR model, which only contains the dominant (2, 2) mode, hardly shows bimodality in most of the parameters, but the posteriors peak away from the true (injected) values. Higher modes can thus be important even when the mass ratio is close to 1, but the spins and total mass are high.

model corresponding to the two maximum likelihood points defined in the regions $q \leqslant 2.5$ (low q) and $q > 2.5$ (high q). To obtain whitened waveforms in the time domain we first divide the waveform in the frequency domain by $\sqrt{S_n(f)}$, and then we inverse Fourier transform them into the time domain. Whitening of the waveforms helps us to better understand the matching of the signal with the waveform, because we can see from Equation (5) that the power spectral density $S_n(f)$ appears inverse weighted in the likelihood function.

From the left panel of Figure 8, we can see that there is a very good agreement between the two whitened waveforms even though the unwhitened waveforms, shown in the right panel of Figure 8, have differences at earlier and earlier times before coalescence. Thus the bimodality appears to stem from a conspiracy: the total mass is very high and hence the number of GW cycles is already just a few within the detectors' bandwidth, and the early cycles of the signals, where they differ significantly, are being suppressed by the worsening of the PSDs.[13] We also compute overlaps using Equation (7) between the maximum likelihood signal and other points from the posterior samples. We find similar bimodal behavior in the distribution of the overlaps. This indicates that there are two points in the parameter space that have a larger match, as we also see visually in the left panel of Figure 8. Moreover, when we recover the signal with just the SEOBNR model, which only contains the (2, 2) mode, we find that it is the high-q region that has the point with the highest posterior probability rather than the low-q region, where actually the injection lies. The S/Ns recovered with the SEOBNR model at the maximum likelihood points in these two regions are pretty close, 19.49 and 19.63, respectively. Note that the injected S/N is 20. Thus, almost all of the S/N is being recovered by the 22 mode waveform, yet the recovered posteriors are significantly different. This suggests that the inclusion of higher modes can matter for inferring the properties of the source (IMBHBs) even when the mass ratio is close to 1, but the spins and the total mass are high. In particular, the global maximum likelihood is still recovered in the region around the injection (low q).

---

[13] However, an unresolved question is why bimodality does not seem to occur when spins $\chi_{1,2} < 0.8$ at high total masses.

4. Upper Stellar-mass Gap

Before discussing the implications of our parameter-estimation study of IMBHB systems for the measurement of the BH's upper stellar-mass gap, we first review the main results in the literature on this topic, and then perform, using updated ^{12}C(α, γ)^{16}O reaction rates, a new study aimed at establishing more robustly the uncertainties in the upper and lower edges of the mass gap.

4.1. What Is the Black Hole Mass Gap?

As mentioned in Section 1, single stars with masses of $20\,M_\odot \lesssim M_{\rm ZAMS} \lesssim 100\,M_\odot$ end their lives in core-collapse supernovae and are thought to exclusively form BHs (Timmes et al. 1996; Fryer & Kalogera 2001; Zhang et al. 2008; Sukhbold & Woosley 2014; Sukhbold et al. 2018). Stars with $M_{\rm ZAMS} \gtrsim 100\,M_\odot$ reach core temperatures of $\gtrsim 7 \times 10^8$ K, which allow for the production of electron–positron pairs from photons, $\gamma + \gamma \rightarrow e^- + e^+$ (Fowler & Hoyle 1964; Barkat et al. 1967; Rakavy & Shaviv 1967). The production of $e^- e^+$ pairs removes photons, softening the equation of state. These stars are expected to become dynamically unstable before core oxygen depletion, as the pair production leads to regions where the adiabatic index $\Gamma_1 = d\ln P/d\ln\rho|_S \leqslant 4/3$ (Fraley 1968; Ober et al. 1983; Bond et al. 1984; Woosley et al. 2002; Heger et al. 2003; Takahashi 2018; Farmer et al. 2019; Marchant & Moriya 2020). The ensuing dynamical collapse results in vigorous oxygen burning whose outcome depends, in part, on the mass of the star and the adopted ^{12}C(α, γ)^{16}O reaction rate.

Stars with $100\,M_\odot \lesssim M_{\rm ZAMS} \lesssim 130\,M_\odot$ can undergo a cyclic pattern of entering the pair instability region: contracting, undergoing oxygen burning, and expanding (Heger et al. 2003; Blinnikov 2010; Chatzopoulos & Wheeler 2012; Yoshida et al. 2016; Woosley 2017; Umeda et al. 2020). This process yields a series of pulsations that remove large amounts of mass from the star, leading to a pulsational pair instability supernova (PPISN) whose core collapse leaves significantly lower-mass BHs. PPISNe set the lower edge of the BH mass gap. The importance of the impact of angular momentum transport was investigated by Marchant & Moriya (2020), and the influence of metallicity, wind mass loss prescription, and treatments of
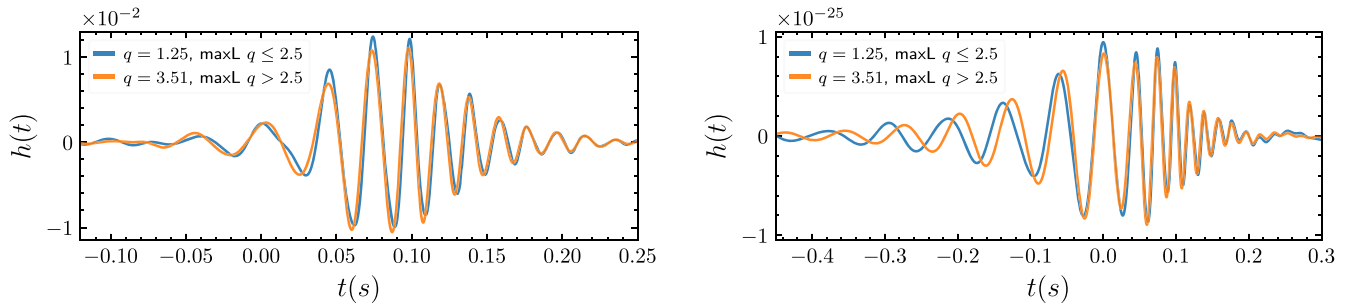
Figure 8. Whitened (left panel) and unwhitened (right panel) strains, at the LIGO–Livingston detector, for the parameters of the two maximum likelihood points of the injection study shown in Figure 7 (for SEOBNRHM–SEOBNRHM model), which is from the region $q \leqslant 2.5$ and $q > 2.5$. The change in amplitude between the two plots reflects the fact that the PSD is $\sim 10^{-46}$ in the band of interest, but is not relevant. What is relevant is the change in the shape of the waveform—the two whitened waveforms match very well (left panel) even though the unwhitened waveforms differ more significantly (right panel) at earlier times.

chemical mixing on the lower edge of the BH mass gap was explored by Farmer et al. (2019).

Stars with $130\,M_\odot \lesssim M_{\mathrm{ZAMS}} \lesssim 250\,M_\odot$ can produce a pair instability supernova (PISN) where the energy injected from the first explosive oxygen-burning event completely unbinds the star (Joggerst & Whalen 2011; Chatzopoulos et al. 2013; Kozyreva et al. 2014; Gilmer et al. 2017; Marchant & Moriya 2020; Renzo et al. 2020). PISNe leave no compact object, making them responsible for the existence of the BH mass gap. Stars with $M_{\mathrm{ZAMS}} \gtrsim 250\,M_\odot$ reach core temperatures of $\log(T_c/\mathrm{K}) \approx 9.8$, where the rate of endothermic photo-disintegration reactions absorbs enough energy to prevent the star from unbinding (Heger et al. 2003). The star, once again, can reach core collapse. This sets the upper boundary of the mass gap.

In addition to the ZAMS mass, the $^{12}\mathrm{C}(\alpha, \gamma)^{16}\mathrm{O}$ reaction rate plays a central role in determining the final outcome by setting the C/O ratio in the core after helium burning. Takahashi (2018) found that cores with reduced $^{12}\mathrm{C}(\alpha, \gamma)^{16}\mathrm{O}$ rates have larger C/O ratios, develop shell convection during central carbon burning, and sufficiently avoid the pulsational-instability regime to collapse as BHs. Farmer et al. (2020) found that cores with reduced $^{12}\mathrm{C}(\alpha, \gamma)^{16}\mathrm{O}$ rates can have C/O ratios $\simeq 0.4$. These cores undergo a sequence of central carbon burning, off-center carbon burning, central oxygen burning, and core collapse to produce a BH. Cores with median $^{12}\mathrm{C}(\alpha, \gamma)^{16}\mathrm{O}$ rates can have C/O ratios $\simeq 0.1$. These cores effectively skip central carbon burning to yield PPISNe with smaller BH masses. Cores with large $^{12}\mathrm{C}(\alpha, \gamma)^{16}\mathrm{O}$ rates can have C/O ratios $\ll 0.1$. These cores effectively skip central and shell carbon burning. They proceed directly to explosive oxygen burning and result in a PISN. Given this sensitivity, we thus undertake a new exploration of the $^{12}\mathrm{C}(\alpha, \gamma)^{16}\mathrm{O}$ reaction rate and its uncertainties.

4.2. Updated $^{12}C(\alpha, \gamma)^{16}O$ Reaction Rates

The C/O content of stellar cores is determined by the competition between triple-α to $^{12}\mathrm{C}$ and $^{12}\mathrm{C}(\alpha, \gamma)^{16}\mathrm{O}$ nuclear reaction rates during helium burning (deBoer et al. 2017). Because of the complexity of the calculations, most analyses have only considered a subset of the reaction channels and a few representative data sets. In order to obtain a comprehensive evaluation, deBoer et al. (2017) considered the entirety of existing experimental data related to the determination of the low-energy $^{12}\mathrm{C}(\alpha, \gamma)^{16}\mathrm{O}$ cross sections, aggregating 60 yr of experimental data consisting of more than 50 independent experimental studies. The more than 10,000 data points were then incorporated into a complete multichannel phenomenological R-matrix analysis

(Lane & Thomas 1958; Azuma et al. 2010; Descouvemont & Baye 2010) using the code AZURE2 (Azuma et al. 2010; Uberseder & deBoer 2015). A main result was the characterization of the uncertainty in the reaction rate, which was accomplished through a Monte Carlo uncertainty analysis of the data and the extrapolation to low energy using the R-matrix model. This resulted in a rate uncertainty that had statistical significance, which had only been accomplished in a few other previous works (e.g., Gialanella et al. 2001; Schürmann et al. 2012), and there with much more limited data sets. In deBoer et al. (2017), the 1σ uncertainty of the reaction rate was given after finding an approximately Gaussian underlying probability distribution for the rate.

In the recent work by Farmer et al. (2020), the main rate that was used was that of Kunz et al. (2002), but with the central value adjusted to be the geometric mean of the upper and lower 1σ uncertainty estimates, with the assumption that these 1σ values reflect an underlying probability distribution that is approximately Gaussian. This modified rate was implemented in the STARLIB rate library (Sallaska et al. 2013). The work of deBoer et al. (2017) was very much in the spirit of that of Kunz et al. (2002), but used a Monte Carlo method to estimate the uncertainties (instead of χ^2) and had at its disposal the significantly increased number of experimental measurements that had accrued in the intervening time. In particular, the significantly more stringent constraints for the values of the sub-threshold asymptotic normalization coefficients were determined through sub-Coulomb transfer measurements (Brune et al. 1999; Avila et al. 2015) and the facilitation of them using the alternative R-matrix parameterization of Brune (2002).

To facilitate the present calculations, and future ones, we expand the tabulated reaction rate to a much finer temperature grid. This is done to ensure that no temperature step results in variations in the rate of more than an order of magnitude. The expanded reaction rates of deBoer et al. (2017) are shown in Figure 9, over a region of $\pm 3\sigma$. As shown previously by Farmer et al. (2020), the uncertainty present in this nuclear reaction rate translates into one of the primary sources of uncertainty in the location of the BH mass-gap boundaries.

4.3. The Black Hole Mass Gap with Updated $^{12}C(\alpha, \gamma)^{16}O$ Reaction Rates

We use MESA version r11701 (Paxton et al. 2011, 2013, 2015, 2018, 2019) to evolve massive helium cores with a metallicity of $Z = 10^{-5}$ until they either collapse to form a BH or explode as a PISN without leaving a compact remnant. We use the same inlists and run_star_extras.f as in

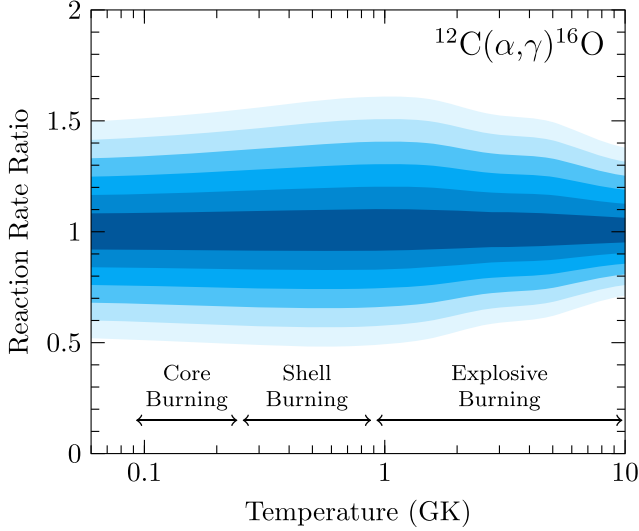**Figure 9.** Relative uncertainties in the $^{12}C(\alpha, \gamma)^{16}O$ reaction rate of this work, expanded from those presented in deBoer et al. (2017). The uncertainties are normalized to the central value for clearer presentation. The regions of fading blue color represent 0.5σ steps in the Gaussian uncertainty distribution.

Farmer et al. (2020) to calculate the boundaries of the BH mass gap with respect to the updated $^{12}C(\alpha, \gamma)^{16}O$ reaction rate uncertainties.

Figure 10 shows the location of the PISN BH mass gap as a function of the uncertainty in the $^{12}C(\alpha, \gamma)^{16}O$ rate. As the reaction rate increases, through increasing $\sigma[^{12}C(\alpha, \gamma)^{16}O]$, both the lower and upper edges of the BH mass gap shift to lower masses while maintaining a roughly constant width, of $\simeq 80^{+9}_{-5} M_\odot$. For the updated $\sigma[^{12}C(\alpha, \gamma)^{16}O]$ rates adopted in this work, the location of the lower and upper edges over the $\pm 3\sigma$ range is $\simeq 59^{+34}_{-13} M_\odot$ and $\simeq 139^{+30}_{-14} M_\odot$ respectively. These results are commensurate with Farmer et al. (2020) at the $\simeq 20\%$ level for the lower edge of the BH mass gap and at the $\simeq 5\%$ level for the upper edge. We next discuss the main reasons why our results differ slightly and put them in context with previous studies.

Marchant & Moriya (2020) found that the efficiency of angular momentum transport changes the lower edge of the BH's mass gap at the $\simeq 10\%$ level. Farmer et al. (2019) found that the lower edge of the mass gap was robust at the $\simeq 10\%$ level to changes in the metallicity, wind mass loss prescription, and treatment of chemical mixing. Our models use twice the mass resolution and about 2.5 times the temporal resolution as those used in Farmer et al. (2020), which we estimate means the results shown in Figure 10 should be robust with respect to mass and temporal resolution at the $\simeq 10\%$ level. For each $\sigma[^{12}C(\alpha, \gamma)^{16}O]$, our $\Delta M = 1 M_\odot$ mass grid of MESA models consumed $\simeq 60,000$ core-hours, with Figure 10 thus costing $\simeq 780,000$ core-hours.

4.4. Sensitivity to the Resolution of the Tabulated $^{12}C(\alpha, \gamma)^{16}O$ Reaction Rates

Within the context of these specific MESA models, Figure 11 shows the dependence of the BH mass spectrum on the tabulated temperature resolution of the $\sigma = 0$ $^{12}C(\alpha, \gamma)^{16}O$ reaction rate at the baseline mass and temporal resolution. When the reaction rate is defined by 52 temperature points, the BH mass spectrum reaches a maximum BH mass of 49.6 $M_\odot$ at
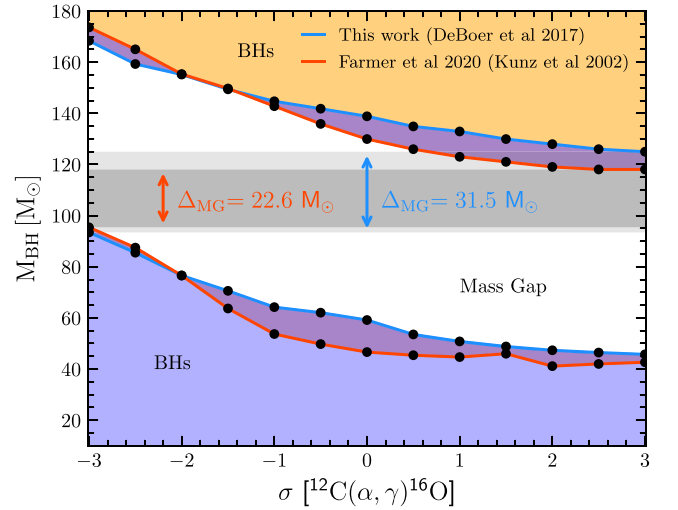
Figure 10. The location of the BH mass gap as a function of the temperature-dependent uncertainty in the $^{12}C(\alpha, \gamma)^{16}O$ reaction rate. The blue lines mark the mass-gap boundaries predicted by our updated $^{12}C(\alpha, \gamma)^{16}O$ rate uncertainties. The orange lines mark the mass-gap boundaries, as found in Figure 5 of Farmer et al. (2020), predicted by the Kunz et al. (2002) rate as expressed in the STARLIB reaction rate library (Sallaska et al. 2013). The white region denotes the mass gap, the purple regions highlight differences in the adopted $^{12}C(\alpha, \gamma)^{16}O$ rates, and the labeled gray horizontal bars denote the mass range where a BH does not form for any value of the adopted $^{12}C(\alpha, \gamma)^{16}O$ rate.
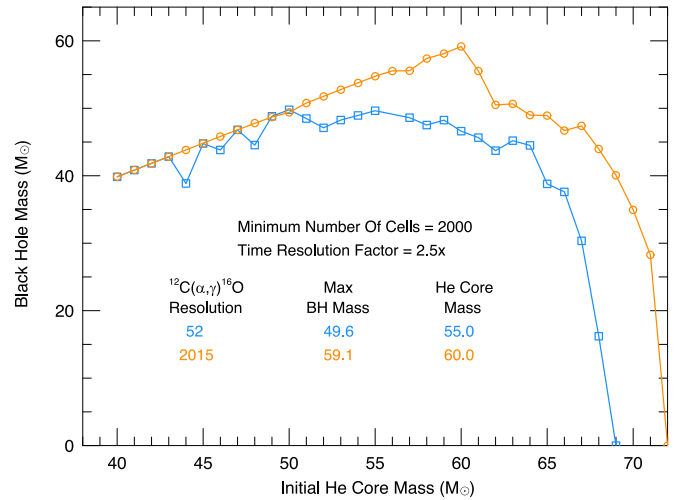
Figure 11. BH mass spectra for different $^{12}C(\alpha, \gamma)^{16}O$ reaction rate resolutions at the adopted baseline mass and temporal resolution. Commonly used reaction rate resolutions of 52 temperature points produce smaller BH masses.

an initial helium core mass of 55.0 $M_\odot$. When the reaction rate is defined by 2015 temperature points, the BH mass spectrum reaches a maximum BH mass of 59.1 $M_\odot$ at an initial helium core mass of 60.0 $M_\odot$. The 52 point rate produces a flatter BH mass spectrum, while the 2015 point rate sustains a linear trend of larger BH masses with larger initial helium core masses until the peak at an initial helium core mass of 60.0 $M_\odot$. Overall, the 52 temperature point rate produces smaller BH masses than the 2015 temperature point rate.

Figure 12 shows why the 52 temperature point reaction rate produces a different BH mass spectrum than the 2015 temperature point reaction rate: the errors from interpolating the 52 temperature point reaction rate are larger than the formal uncertainties in the 2015 temperature point reaction rate. Fundamentally, the 52
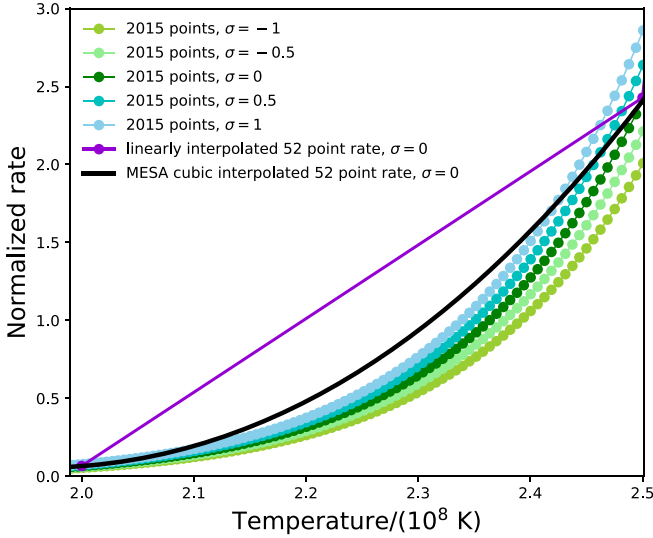
Figure 12. The 2015 temperature point $\sigma = 0$, ± 0.5, and ± 1.0 normalized ^{12}C $(\alpha,\gamma)^{16}$O reaction rate (green/blue curves) over the relevant temperature range for helium burning. Also shown is the reaction rate that results from linearly interpolating the $\sigma = 0$ rate defined by 52 temperature points (purple curve) and the reaction rate from MESA's cubic interpolation of the $\sigma = 0$ rate defined by 52 temperature points (black curve). The error from interpolating the 52 temperature point $\sigma = 0$ rate is larger than the $\sigma = +1.0$ rate defined by 2015 temperature points.

Figure 13. Evolution of the central ^{12}C mass fraction with core temperature for the $M_{\mathrm{He,init}} = 60\ M_\odot$ stellar models. The color scheme is the same as in Figure 12. The 52 temperature point $\sigma = 0$ reaction rate yields a smaller central carbon mass fraction than the 2015 temperature point $\sigma = 0$ reaction rate.

temperature point reaction rate is "bad" because the reaction rate changes by nearly an order of magnitude between tabulated temperature points. When a reaction rate varies by this much between tabulated temperature points, there is a limit to what interpolation can provide.

Delving deeper, Figure 13 shows the evolution of the central ^{12}C mass fraction from near the onset of helium ignition to central carbon ignition for the $M_{\mathrm{He,init}} = 60\ M_\odot$ stellar model as a function of the central temperature (a proxy for time). The model computed with the 52 temperature point $\sigma = 0$ reaction rate achieves a central carbon mass fraction of ~ 0.125. Stellar models computed using the 2015 temperature point $\sigma = 0$ reaction rate achieve a central carbon mass fraction of ~ 0.17. This difference in the carbon mass fraction of the core is the primary reason why the BH mass spectra shown in Figure 11 differ.

We also calculate new $\pm 3\sigma$ rates for the ^{12}C + ^{12}C, ^{12}C + ^{16}O, and ^{16}O + ^{16}O reactions. Consistent with Farmer et al. (2020), we find that these reaction rates move the BH's mass-gap boundary by $\lesssim 1\ M_\odot$. Evidently, in this case, the total energy liberated by C-burning is more important than how quickly or slowly this energy is liberated. A large carbon fuel reservoir from a small ^{12}C$(\alpha, \gamma)^{16}$O rate leads to a more massive BH, an intermediate carbon fuel reservoir from the recommended (i.e., median) ^{12}C$(\alpha, \gamma)^{16}$O rate leads to less massive BHs, and a small carbon mass fraction from a large ^{12}C$(\alpha, \gamma)^{16}$O rate leads to no compact object being formed (i.e., a PISN).

4.5. Sensitivity to Mass and Time Resolution

Figure 14 shows the impact of enhanced time and mass resolution on the BH mass spectrum. The first spectrum, labeled (a), is calculated as in Farmer et al. (2020) with the MESA controls: `max_dq = 1d-3` and `delta_lgRho_cntr_limit = 2.5d-3`. The `max_dq` control limits the mass of any given cell to contain
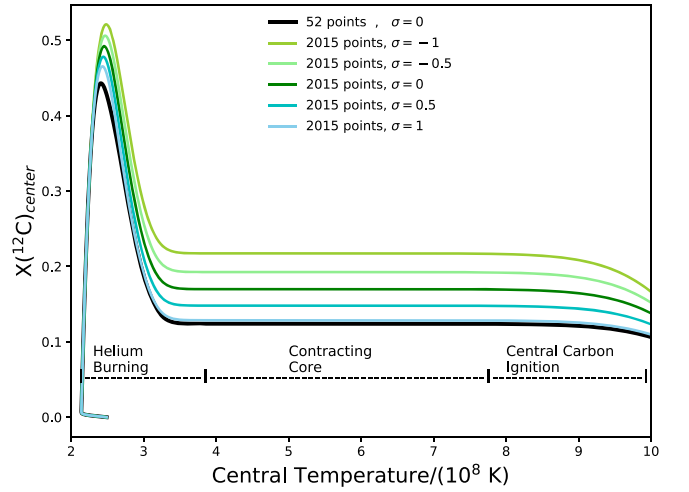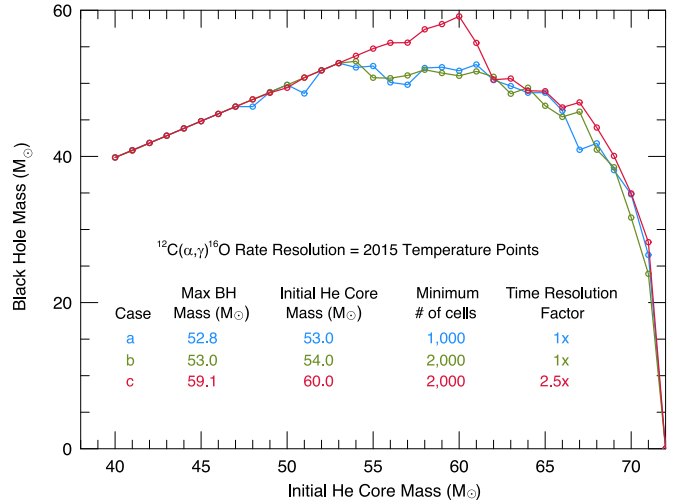
Figure 14. Black hole mass spectrum for different mass and time resolutions at the highest ^{12}C$(\alpha, \gamma)^{16}$O reaction rate resolution. Increasing the mass resolution (olive curve) does not appreciably change the spectrum, while increasing the time resolution (red curve) allows the linear trend at low initial helium core masses to continue to $\simeq 60\ M_\odot$.

no more than the specified fraction of the total mass. That is, the minimum number of cells in a model is $1/$max_dq. The `delta_lgRho_cntr_limit` limits the size of time steps such that the central density does not change by more than a specified fraction. The second BH mass spectrum, labeled (b), doubles the mass resolution by halving `max_dq`, implying a minimum of 2000 cells. The third BH mass spectrum, labeled (c), increases the temporal resolution by a factor of 2.5 by decreasing `delta_lgRho_cntr_limit` by the same factor.

Increasing the mass resolution of our models yields little discernible difference in the BH mass spectrum: compare case (a) versus case (b) in Figure 14. Increasing the temporal resolution, case (c), increases the maximum BH mass in the BH mass spectrum from 53.0 $M_\odot$ in case (b) to 59.2 $M_\odot$ in case (c). This difference is due to the smaller time steps allowing the pressure-weighted volume average $\langle \Gamma_1 \rangle$ to get closer to 4/3 without dipping below it. See Stothers (1999) and Farmer et al. (2020) for a discussion of $\langle \Gamma_1 \rangle$. This allows convective carbon shell burning to
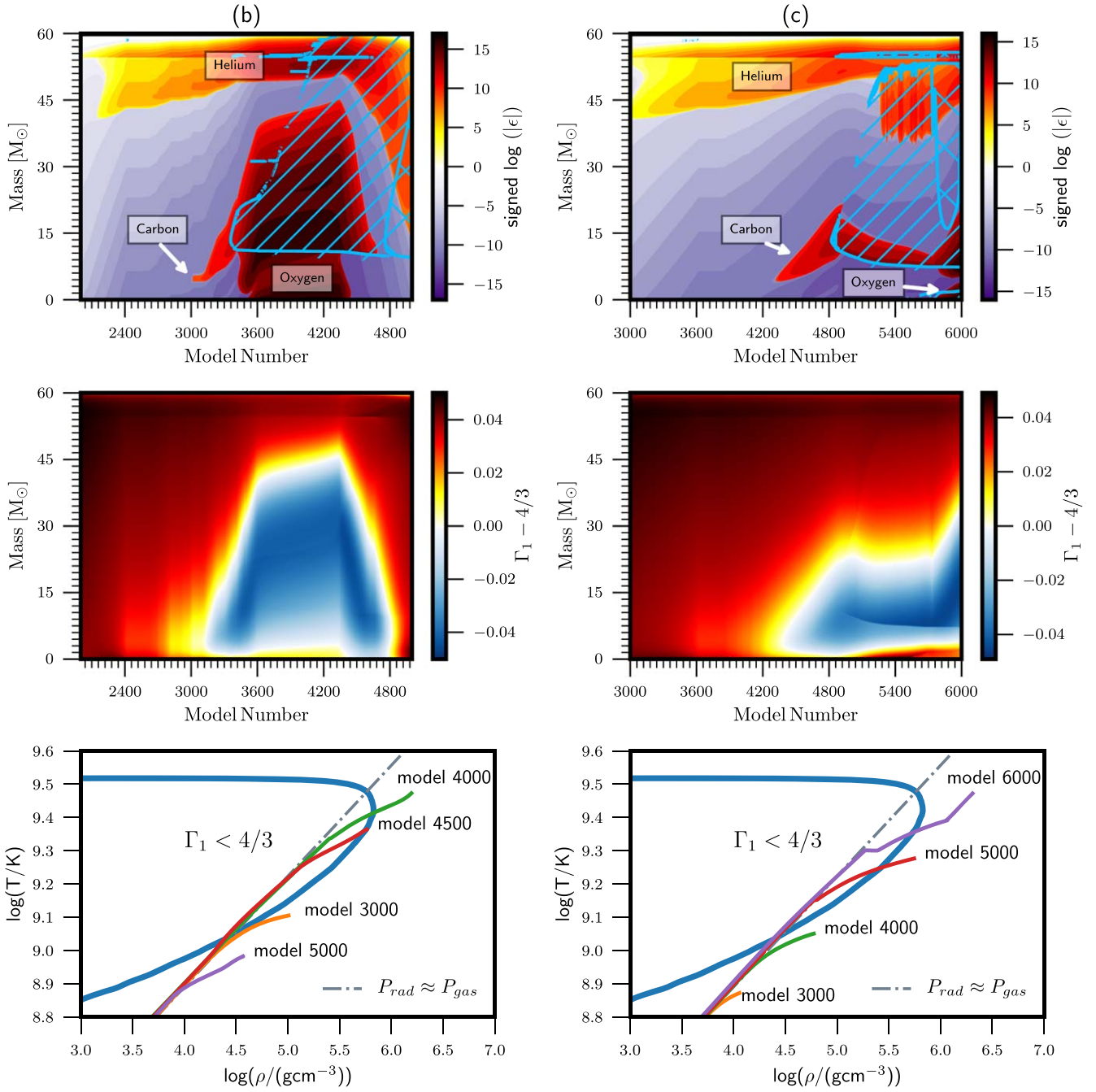
Figure 15. Evolution of $M_{\mathrm{He,init}} = 60\,M_\odot$ models for time resolutions of case (b) and case (c); also see Figure 4 of Farmer et al. (2020). The purpose of the figure is to highlight the difference in carbon ignition between two stellar models, not to show the evolution of a full pulsation cycle in each model. The top row shows the signed logarithm of the net specific power, $\mathrm{sign}(\epsilon_{\mathrm{nuc}} - \epsilon_\nu)\log_{10}(\max(1.0, |\epsilon_{\mathrm{nuc}} - \epsilon_\nu|))$, where ϵ_{nuc} is the specific energy generation rate and ϵ_ν is the specific energy loss from neutrinos. Purple regions denote strong neutrino cooling and red regions denote regions of strong nuclear burning. Positive sloped blue hatched regions indicate standard mixing length convection; negatively sloped blue hatched regions indicate convection with no mixing. The different fuels burning are labeled. The middle row shows the evolution of locally unstable regions with $\Gamma_1 < 4/3$. The bottom row shows the density–temperature structure for different model numbers. The dashed line shows where the gas pressure is equal to the radiation pressure. The solid blue curve encloses the $\Gamma_1 < 4/3$ region. When pressure-weighted volume average $\langle\Gamma_1\rangle$ drops below $4/3$ the model becomes dynamically unstable.

take place before core oxygen ignition. For carbon mass fractions $\gtrsim 0.17$, off-center carbon burning is strong enough to trigger convective mixing and burning of the entire carbon shell, preventing the model from reaching the $\langle\Gamma_1\rangle$ instability. The model stabilizes long enough for the core to burn a significant fraction of its oxygen before $\langle\Gamma_1\rangle$ dips below $4/3$. In turn, this allows the stellar interior to progress closer to core collapse before the $\langle\Gamma_1\rangle$ instability coupled with oxygen burning triggers a pulse of mass loss. We conclude that for models with carbon mass

fractions $\gtrsim 0.17$, smaller time steps are necessary to resolve the peak of the BH mass spectrum, although additional time resolution could be necessary at lower mass fractions.

Figure 15 shows the evolution of the internal structure of an $M_{\mathrm{He,init}} = 60\,M_\odot$ model for the time resolutions of case (b) and case (c) explored in Figure 14. Both models highlight an episode of radiative carbon burning in the core, followed by convective carbon burning in a shell. However, the two time resolutions show different evolutions of carbon shell burning.

In the case (b) model, carbon ignition occurs near model 3000, $\tau_{ci} = 0$ hr where τ_{ci} is the time after carbon ignition. Carbon shell burning generates a small convective region starting at about model 3400, $\tau_{ci} \simeq 470$ hr. Only a portion of the carbon shell is burned before $\langle \Gamma_1 \rangle < 4/3$, which occurs near model 3430, $\tau_{ci} \simeq 477$ hr. Oxygen ignites radiatively in the core at about model 3500, about 0.06 hr later. The energy release from helium burning as a result of helium mixing deep into the structure in the $\simeq 60$ s between models 4500 and 5000 is $\simeq 10^{41}$ erg. This is $\simeq 7$ orders of magnitude smaller than the change in the total energy over the same model numbers, suggesting the integrated energy release is dynamically small. Oxygen burning causes a pulse of mass loss that removes $\simeq 5\,M_\odot$ of material from the surface layers by about model 8000, $\tau_{ci} \simeq 757$ hr (not shown in Figure 15). A second pulse then removes an additional $\simeq 3\,M_\odot$ of material from the surface layers at about model 16,000, about 1940 yr later (not shown in Figure 15).

In the case (c) model, carbon ignition occurs near model 4400, $\tau_{ci} = 0$ hr. Carbon shell burning becomes strong enough to grow the convective region, mixing the entire shell starting at model 4800, $\tau_{ci} \simeq 240$ hr, and ending at model 5300, $\tau_{ci} \simeq 351$ hr. This allows the model to stave off the $\langle \Gamma_1 \rangle$ instability until the carbon mass fraction in the shell drops to $\simeq 10\%$ of its initial value near model 5780, $\tau_{ci} \simeq 388$ hr. Only then does the model become dynamically unstable to $\langle \Gamma_1 \rangle < 4/3$. A weak pulse then removes $\simeq 0.3\,M_\odot$ of material from the surface layers by about model 11,500, $\tau_{ci} \simeq 433$ hr (not shown in Figure 15).

The difference in the final BH mass for the two different time resolutions is the result of a tight coupling between the nuclear burning and convection. Smaller time steps better resolve the coupling. These results suggest a more extensive convergence study may be needed to accurately resolve the peak of the BH mass spectrum.

4.6. Measurement of Mass Gap with Upcoming LIGO–Virgo Observations

Figure 10 shows that at the median ($\sigma = 0$) of the ^{12}C$(\alpha, \gamma)^{16}$O reaction rate, the mass gap would typically fall in the range 60–130 $M_\odot$ considering the overlapping parts of the range from the two ^{12}C$(\alpha, \gamma)^{16}$O rates. Including such a range in Figures 5 and 6 (see shaded gray region), we find that the uncertainties in the primary-mass measurements for asymmetric IMBHB systems are $\sim 17\%$–25%, while for nearly symmetric systems they are $\sim 30\%$–50%. For the latter systems, the secondary mass also quite often falls in the mass gap, and can be constrained with an uncertainty of $\sim 40\%$–70%.

How confidently will the upcoming O4 run be able to identify that the component masses of IMBHB systems lie in the mass gap? To address this question we need to account for the uncertainties in the boundaries of the mass gap shown in Figure 10, which are caused by uncertainties in the ^{12}C$(\alpha, \gamma)^{16}$O rate. The probability that a component mass of the IMBHB system lies in the mass gap can be computed as

$$P(\mathrm{MG}) = P(m_{\mathrm{MG}}^{\mathrm{L}} < m_i^s < m_{\mathrm{MG}}^{\mathrm{U}}),$$
$$= \int P(x)dx \int_{m_{\mathrm{MG}}^{\mathrm{L}}(x)}^{m_{\mathrm{MG}}^{\mathrm{U}}(x)} P(m_i^s|d)dm_i^s, \quad (12)$$

where $i = 1, 2$, x denotes the ^{12}C$(\alpha, \gamma)^{16}$O rate, $m_{\mathrm{MG}}^{\mathrm{L}}$ and $m_{\mathrm{MG}}^{\mathrm{U}}$ denote the lower and upper edges of the mass gap, and d represents the data (i.e., the simulated GW signal). We can approximate the above equation as a discrete sum in x:

$$P(\mathrm{MG}) = P(m_{\mathrm{MG}}^{\mathrm{L}} < m_i^s < m_{\mathrm{MG}}^{\mathrm{U}}),$$
$$= \sum_{j=1}^{N=13} P(x_j) \int_{m_{\mathrm{MG}}^{\mathrm{L}}(x_j)}^{m_{\mathrm{MG}}^{\mathrm{U}}(x_j)} P(m_i^s|d)dm_i^s, \quad (13)$$

where j runs from 1 to the 13 grid points of the ^{12}C$(\alpha, \gamma)^{16}$O reaction rate shown in Figure 10 and $P(x_j)$ is the corresponding probability.[14]

If $P(\mathrm{MG})$ is large, then the source could be a mass-gap event. However, events that are not in the mass gap will occasionally have large $P(\mathrm{MG})$ simply due to noise fluctuations. Thus, the probability necessary to claim a confident detection of a mass-gap event depends on the relative rate of mass-gap and no-mass-gap events. To test the hypothesis that there are events with components in the mass gap, we should compute the Bayesian evidence for the no-mass-gap versus mass-gap hypotheses, marginalized over the uncertain proportion of events that are in the mass gap. This approach leverages information from all events, not just those with high $P(\mathrm{MG})$, and therefore has greater statistical power. However, such an analysis is beyond the scope of the current paper. Here we will only compute $P(\mathrm{MG})$ for noise-free data with a variety of injected IMBHB systems. Signals with high $P(\mathrm{MG})$ are more likely to be robustly identified as mass-gap events, but we warn the reader against overinterpreting our numbers.

We show in Figure 16 $P(\mathrm{MG})$ for IMBHB systems with primary mass $m_1^s = [70, 80, 90, 110, 120]\,M_\odot$ and several spin values, observed at an inclination angle of $\pi/3$, computed using the updated ^{12}C$(\alpha, \gamma)^{16}$O rate. As we can see, for asymmetric IMBHB systems (i.e., $q > 1.25$), if the primary mass is well within the median mass gap (e.g., $m_1^s \in [80, 120]\,M_\odot$), then the primary mass has a probability of being in the mass gap $> 95\%$ (i.e., a single observation could be sufficient to robustly identify the existence of sources in the mass gap). For systems with primary mass close to the lower edge of the median mass gap (e.g., $m_1^s \sim 70 M_\odot$), $P(\mathrm{MG})$ reduces to ~ 0.85 for antialigned systems. For nearly symmetric IMBHB systems (i.e., $q = 1.25$), $P(\mathrm{MG}) > 95\%$ for systems with somewhat higher primary mass, namely, $m_1^s \gtrsim 85\,M_\odot$. Symmetric systems can also have a high probability that the secondary mass lies in the mass gap. The right panel in Figure 16 indicates that for IMBHB systems with $m_2^s \in [90, 120]\,M_\odot$, the posterior probability that the secondary mass lies within the mass gap exceeds 90% for systems with $\chi_{1,2} < 0.80$. By contrast, high-spin systems with $\chi_{1,2} > 0.80$ exhibit bimodality, which worsens the precision of the mass measurement, as discussed in Section 3.3.

For IMBHBs at zero inclination angle (face-on), our study shows that $P(\mathrm{MG})$ is generally lower for measurements of the primary mass, reaching values as low as ~ 0.6 in some cases (e.g., at the upper edge of the mass gap $\sim 120\,M_\odot$, where bimodality occurs). Nonetheless, systems with $m_1^s \in [80, 110]\,M_\odot$ would

---

[14] We compute these probabilities from the standard normal distribution, evaluated at the given σ uncertainty, and then renormalize them so that they add up to 1. Alternatively, one could interpolate between these grid points and make the approximation in Equation (13) more and more precise by increasing N, but we do not expect that the results will change very significantly.
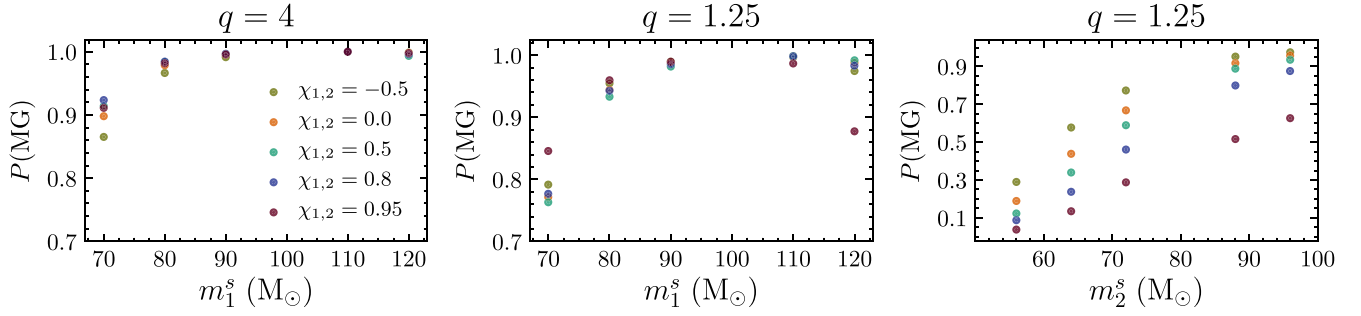
Figure 16. Probability of being in the BH's mass gap (see Equation (13)) as a function of source-frame component masses for several IMBHB systems with primary mass $m_1^s = [70, 80, 90, 110, 120]$ $M_\odot$ and different spin values (as illustrated in the legend in the left panel), at an inclination angle of $\pi/3$ and S/N of 20. Results are obtained using the spinning, nonprecessing SEOBNRHM model. Independently of the mass ratio, when IMBHBs have primary mass in the range [80, 120] $M_\odot$, the signal can be identified as a BH in the mass gap with probability >90%.
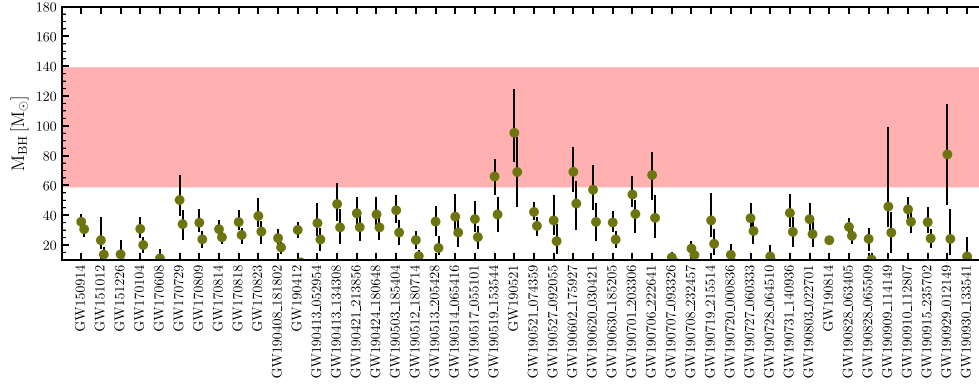
Figure 17. The source-frame component masses and their associated 90% credible intervals of all events from GWTC-1 and GWTC-2 with the restriction that the median estimated mass of the primary is $\geqslant 10$ $M_\odot$. The red region shows the mass gap at $\sigma = 0$ for the updated ^{12}C$(\alpha, \gamma)^{16}$O rate (see Figure 9). The primary mass of the GW190521 event along with its associated 90% credible interval lies well inside the red region, indicating that this could be a BH in the mass gap. Our reanalysis of GW190521 in Section 4.7 confirms this result with the waveform models used in this work. We note that there are also five more component masses, including the secondary mass of GW190521, whose posterior-distribution medians lie in the mass gap.

still yield $P(\mathrm{MG})$ exceeding ~0.8. Measurements of the secondary mass only provide $P(\mathrm{MG}) > 0.8$ when the binary system has $m_2^s > 90$ $M_\odot$.

4.7. Reanalysis of GW190521

As discussed in Section 1, Abbott et al. (2020b) reported the detection of the first IMBHB system, namely GW190521. Using spinning, precessing waveform models, the primary mass of GW190521 was estimated to lie in the mass gap [65, 120] $M_\odot$ with probability above 99%, i.e., $P(\mathrm{MG}) > 0.99$ (see this event in Figure 17), when using the NRSurPHM model. When taking into account the uncertainty in the mass-gap boundary itself (see Equation (13)), we still find that the probability is above 98%. Recently, Nitz & Capano (2021) reanalyzed GW190521 using the spinning, precessing waveform model PhenomPHM (Pratten et al. 2021),[15] which was not employed in Abbott et al. (2020b). They extended the priors on the mass ratio, observed multimodality in the component masses, and also found that the maximum likelihood parameter lies at high mass ratio, $q \sim 10$, indicating that the event might be an inspiral with intermediate mass ratio. Using their public data, namely the results with the prior flat in the source-frame component masses, we find that their results would lead to a probability that the primary mass of GW190521 is in the mass

gap of 55%. We shall comment again on the results of Nitz & Capano (2021) at the end of this section.

Here, we reanalyze GW190521, but mainly with the spinning, nonprecessing SEOBNRHM and PhenomHM waveform models used in this work. We employ the same settings as used for the results publicly released by LIGO and Virgo (Vallisneri et al. 2015; GWOSC 2020; Abbott et al. 2021d), except for two modifications: (i) we extend the prior ranges in the component masses and the mass ratio, and (ii) we use a luminosity distance prior uniform in comoving volume (see Equation (10)). We show the results in Figure 18. With nonprecessing waveforms, we find bimodality in the posterior distributions of some parameters—for example, in the mass of the secondary component (m_2), the luminosity distance (d_L), and the total mass (M_{tot}). However, the posteriors of the source-frame component masses ($m_{1,2}^s$) do not show bimodality. Our nonprecessing analysis also shows that irrespective of the waveform used, the posterior probability for the primary mass to lie in the mass gap is ~99%, while the posterior probability that the secondary mass lies in the mass gap is ~52%.

Furthermore, to contrast the results from the nonprecessing waveforms with the precessing case, we analyze GW190521 with the PhenomPHM model. We note that after the paper by Nitz & Capano (2021) came out, it was realized that the PhenomPHM model had an issue in modeling properly the merger–ringdown waveforms of spinning BBHs when the primary spin is (close to) antialigned with the orbital angular momentum at merger. Here, we first perform our analysis with

---

[15] In LAL this waveform model is denoted IMRPhenomXPHM (Pratten et al. 2021).
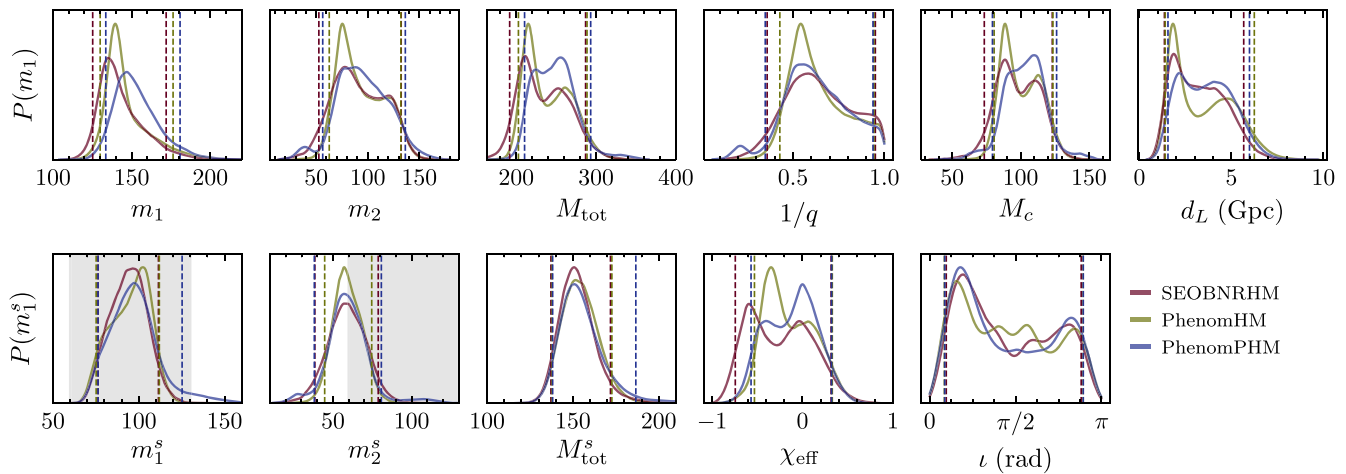
Figure 18. Posterior distributions of the parameters for the GW190521 event observed by LIGO and Virgo detectors (Abbott et al. 2021b, 2021c). The parameter M_f^s and a_f denote the mass and spin of the remnant BH, while the other parameters have been introduced in Section 2.1. The vertical dashed lines in each plot indicate the 90% credible interval for each posterior shown by the same color. The shaded region represents the BH's mass gap of [60, 130] $M_\odot$ derived in Section 4.2 and computed at the median of the $^{12}C(\alpha, \gamma)^{16}O$ reaction rate (see Figure 10). The nonprecessing SEOBNRHM and PhenomHM models do not show bimodality in the source-frame masses $m_{1,2}^s$, while the precessing PhenomPHM model shows additional small bumps in the secondary-mass posterior at $m_2^s \sim 30\,M_\odot$ and $m_2^s \sim 110\,M_\odot$. Except for the latter, there is good agreement between the results of nonprecessing and precessing waveforms, and the 90% credible interval of the primary-mass posterior lies inside the mass gap in all cases.

the same version of the PhenomPHM model used by Nitz & Capano (2021), and find full agreement with their results. Then, we reanalyze GW190521 with the new publicly released version of PhenomPHM. We display the results in Figure 18. As can be seen, the posteriors with the precessing PhenomPHM waveforms show an additional peak, though small, at, e.g., $q \sim 5$ in the mass ratio. The secondary source-frame mass posterior, however, has two additional small bumps at $m_2^s \sim 30\,M_\odot$ and $m_2^s \sim 110\,M_\odot$. Besides those differences, the agreement between the posteriors from the precessing and nonprecessing waveforms is quite good. With the precessing PhenomPHM model in Figure 18, we find that $P(MG)$ is $\sim 98\%$ for the primary mass and $\sim 54\%$ for the secondary mass. To further understand the robustness of these findings, we are currently finalizing a comprehensive analysis with other waveform models with spin precession, namely the time-domain spinning, precessing model from the EOB family (Ossokine et al. 2020). Moreover, such an analysis has also been carried out with a new time-domain phenomenological IMR model in Estellés et al. (2021). With their default version of the new time-domain IMR model, Estellés et al. (2021) reports 91.6% probability for the primary mass to be in the mass gap by simply integrating the primary mass posterior in the range [70, 161]. Their analysis employs a similar prior setting to ours. Our posteriors yield $\sim 99\%$ probabilities when we also integrate them in the mass gap range [70, 161]. Thus, the frequency-domain waveforms used in this section also do a good job as far as the interpretation of the primary mass is concerned.

5. Conclusions

In this paper, we used the spinning, nonprecessing SEOBNRHM waveform model to estimate the precision with which the parameters of nonprecessing IMBHBs could be estimated in the upcoming LIGO–Virgo O4 and O5 runs. We simulated IMBHBs for total detector-frame masses in the range $M_{tot} = [50, 500]\,M_\odot$, mass ratios $q = \{1.25, 4, 10\}$, and component spins $\chi_1 = \chi_2 = [-0.8, 0.95]$ at an S/N of 20. We showed that for binaries with high mass ratio and relatively

high inclination ($\iota = \pi/3$), the mass of the heavier component (i.e., the primary BH) can be constrained with an uncertainty $\sim 11\%-25\%$. These precisions are much better than what is expected from electromagnetic observations. We also showed that the total source mass of IMBHBs can be constrained with uncertainties $\sim 10\%-30\%$, independently of the parameters of the IMBHB systems. These results suggest that future LIGO and Virgo observations hold the potential to measure the mass function of IMBHs and IMBHBs, which remains an important open question in astrophysics.

We also focused on IMBHB systems whose component BHs fall in the upper stellar-mass gap, which is predicted from stellar evolution theory for massive stars. We first studied the sensitivity of the mass-gap edges to the uncertainties in the most relevant nuclear rates, such as $^{12}C(\alpha, \gamma)^{16}O$, $^{12}C + ^{12}C$, and $^{16}O + ^{16}O$, using MESA. We confirmed the results of Farmer et al. (2020) that the boundaries of the mass gap are dependent on the $^{12}C(\alpha, \gamma)^{16}O$ rate, e.g., the lower edge of the mass gap can vary between ~ 40 and $90\,M_\odot$ while the upper edge can lie anywhere between ~ 125 and $170\,M_\odot$. The other nuclear rates, $^{12}C + ^{12}C$, $^{12}C + ^{16}O$, and $^{16}O + ^{16}O$, move the BH mass-gap boundary by only $\lesssim 1\,M_\odot$. The main difference between our results (Figure 10) and Farmer et al. (2020) is at the $\simeq 20\%$ level for the lower edge of the BH mass gap and at the $\simeq 5\%$ level for the upper edge. This is primarily due to the increased resolution of the tabulated $^{12}C(\alpha, \gamma)^{16}O$ reaction rate and the increased temporal resolution of our calculations.

Having updated the boundaries of the mass gap, we analyzed a few IMBHB systems with component masses in the most probable range of the mass gap, and computed the posterior probability of them being in the mass gap based on their single-event observations. We found that for asymmetric inclined IMBHBs whose primary component mass m_1^s lies in the range [80, 120] $M_\odot$, the posterior probability, $P(MG)$, that the primary mass lies in the mass gap is $\gtrsim 95\%$. For symmetric inclined IMBHBs, the same holds when $m_1^s \in [85, 120]\,M_\odot$. Lowering the inclination reduces the precision of the mass measurement, and hence the posterior probability of being in the mass gap decreases. However, face-on IMBHBs with $m_1^s \in [80, 110]\,M_\odot$

would still yield $P(MG)$ exceeding ~ 0.8; systems with $m_1^s \sim 120\, M_\odot$ and high spins fall within the parameter space where bimodality occurs (see Section 3.3) and hence the precision (width) of the mass posteriors decreases (increases). The secondary mass can also fall in the mass gap, especially when the mass ratio of the IMBHBs is near one ($q \sim 1$). However, since the measurement of the secondary mass is relatively poor, $P(MG) > 0.9$ can be achieved only when the secondary mass lies far above the lower edge of the mass gap, $m_2^s \in [90, 120]\, M_\odot$, given also that the inclination is higher.

Within this context, we reanalyzed the GW190521 event with spinning, nonprecessing waveforms SEOBNRHM and PhenomHM and also with the latest version of (frequency-domain) precessing PhenomPHM waveform. We found that there is a very good agreement between the results of nonprecessing and precessing waveforms, at least for the source-frame component masses, which we are interested in. However, the precessing PhenomPHM waveform shows two additional, though really small, bumps in the secondary source-frame component mass (m_2^s). We showed that $P(MG)$ for the primary mass (m_1^s) with the nonprecessing waveforms is $\sim 99\%$ while with the precessing waveform it is $\sim 98\%$. $P(MG)$ for the secondary mass is $\sim 52\%$ with the nonprecessing waveforms, while with the precessing waveform it increases a bit, to $\sim 54\%$, because one of the additional bumps occurs in the mass gap. To complete the reanalysis of GW190521 with state-of-the-art precessing waveforms, we are further investigating this event with more accurate (when compared to numerical-relativity simulations) waveforms, notably the time-domain spinning, precessing model from the EOB family (Ossokine et al. 2020) (see also Estellés et al. 2021, which uses a new time-domain phenomenological model). We further note that the posterior probabilities were obtained using our default priors (see Section 2.2.2), notably priors flat in detector-frame component masses and uniform in comoving volume for the luminosity distance. Employing different priors may change the results.

Furthermore, the probability $P(MG)$ is a guide to how confidently an event can be identified as being a mass-gap event, but the number should not be overinterpreted, as noise fluctuations can lead to large $P(MG)$ for events that are not in the mass gap. The value required for an event to be confidently identified as being a mass-gap event depends on the relative, and unknown, rates of events inside and outside the mass gap. To properly address the question of how many events would be required for a robust identification of a mass-gap population, would require a Bayesian model comparison between a "mass-gap" model and a "no-mass-gap model," using all observed events. We leave this work for future studies. However, systems with high $P(MG)$ are more likely to be robustly identified as mass-gap events.

We note that in this analysis we have not included the KAGRA detector, because it is currently uncertain at what sensitivity KAGRA will be contributing to the network during the O4 and O5 runs (Abbott et al. 2020a). Adding an additional detector of comparable sensitivity will improve parameter estimation by increasing the observed S/N and breaking parameter degeneracies. In the context of IMBH observations, we expect that KAGRA will bring a modest improvement in the precision of the luminosity distance, allowing a slightly better determination of the intrinsic mass, which could facilitate the identification of sources in the mass gap. However, such improvements will be much smaller than the uncertainties in the location of the mass gap described in this manuscript.

The inference studies in this work were limited to multipolar spinning, nonprecessing quasi-circular waveform models, although we performed an analysis where we injected mildly precessing quasi-circular signals and found that the measurement uncertainties on the component masses only changed by $\sim 5\%$ when recovering those signals with nonprecessing waveforms. In view also of possible multimodal posterior distributions for IMBHB systems, we plan in the future to carry out a comprehensive investigation using a larger set of injections of spinning, precessing signals and recover them with precessing (instead of nonprecessing) waveforms. Furthermore, it will be crucial to extend the parameter-estimation study to IMBHBs moving on eccentric orbits. Indeed, given the shortness of IMBHB signals, all physical effects need to be included to avoid misinterpreting the properties of the source (Romero-Shaw et al. 2020; Calderón Bustillo et al. 2021). Recently, a few examples of multipolar spinning, nonprecessing waveform models with mild eccentricity have been developed (Khalil et al. 2021; Liu et al. 2021; Nagar et al. 2021; Yun et al. 2021) that could be used for such studies.

ORCID iDs

Ajit Kumar Mehta ⏺ https://orcid.org/0000-0002-7351-6724
Alessandra Buonanno ⏺ https://orcid.org/0000-0002-5433-1409
Jonathan Gair ⏺ https://orcid.org/0000-0002-1671-3668
M. Coleman Miller ⏺ https://orcid.org/0000-0002-2666-728X

Ebraheem Farag ⬤ https://orcid.org/0000-0002-5794-4286
R. J. deBoer ⬤ https://orcid.org/0000-0003-3784-6360
M. Wiescher ⬤ https://orcid.org/0000-0002-3409-3319
F. X. Timmes ⬤ https://orcid.org/0000-0002-0474-159X

References

Aasi, J., Abbott, B. P., Abbott, R., et al. 2015, CQGra, 32, 074001
Abbott, B. P., Abbott, R., Abbott, T. D., et al. 2017a, PhRvL, 119, 161101
Abbott, B. P., Abbott, R., Abbott, T. D., et al. 2017b, ApJL, 848, L12
Abbott, B. P., Abbott, R., Abbott, T. D., et al. 2017c, Natur, 551, 85
Abbott, B. P., Abbott, R., Abbott, T. D., et al. 2017d, PhRvD, 96, 022001
Abbott, B. P., Abbott, R., Abbott, T. D., et al. 2018, PhRvL, 121, 161101
Abbott, B. P., Abbott, R., Abbott, T. D., et al. 2019a, PhRvX, 9, 031040
Abbott, B. P., Abbott, R., Abbott, T. D., et al. 2019b, PhRvD, 100, 064064
Abbott, B. P., Abbott, R., Abbott, T. D., et al. 2020a, LRR, 23, 3
Abbott, B. P., Abbott, R., Abbott, T. D., et al. 2021a, ApJ, 909, 218
Abbott, R., Abbott, T. D., Abraham, S., et al. 2020b, PhRvL, 125, 101102
Abbott, R., Abbott, T. D., Abraham, S., et al. 2020c, ApJL, 900, L13
Abbott, R., Abbott, T. D., Abraham, S., et al. 2021b, ApJL, 913, L7
Abbott, R., Abbott, T. D., Abraham, S., et al. 2021c, PhRvX, 11, 021053
Abbott, R., Abbott, T. D., Abraham, S., et al. 2021d, SoftX, 13, 100658
Acernese, F., Agathos, M., Agatsuma, K., et al. 2015, CQGra, 32, 024001
Amaro-Seoane, P., Gair, J. R., Freitag, M., et al. 2007, CQGra, 24, R113
Antonini, F., Gieles, M., & Gualandris, A. 2019, MNRAS, 486, 5008
Avila, M. L., Rogachev, G. V., Koshchiy, E., et al. 2015, PhRvL, 114, 071101
Azuma, R. E., Uberseder, E., Simpson, E. C., et al. 2010, PhRvC, 81, 045805
Barkat, Z., Rakavy, G., & Sack, N. 1967, PhRvL, 18, 379
Belczynski, K., Buonanno, A., Cantiello, M., et al. 2014, ApJ, 789, 120
Blinnikov, S. I. 2010, PAN, 73, 604
Bond, J. R., Arnett, W. D., & Carr, B. J. 1984, ApJ, 280, 825
Brown, G. E., Heger, A., Langer, N., et al. 2001, NewA, 6, 457
Brune, C. R. 2002, PhRvC, 66, 044611
Brune, C. R., Geist, W. H., Kavanagh, R. W., & Veal, K. D. 1999, PhRvL, 83, 4025
Buchmann, L. R., & Barnes, C. A. 2006, NuPhA, 777, 254
Bustillo, J. C., Sanchis-Gual, N., Torres-Forné, A., et al. 2021, PhRvL, 126, 081101
Calderón Bustillo, J., Sanchis-Gual, N., Torres-Forné, A., & Font, J. A. 2021, PhRvL, 126, 201101
Campanelli, M., Lousto, C. O., & Zlochower, Y. 2006, PhRvD, 74, 041501
Chatzopoulos, E., & Wheeler, J. C. 2012, ApJ, 760, 154
Chatzopoulos, E., Wheeler, J. C., & Couch, S. M. 2013, ApJ, 776, 129
Costa, G., Bressan, A., Mapelli, M., et al. 2021, MNRAS, 501, 4514
Cotesta, R., Buonanno, A., Bohé, A., et al. 2018, PhRvD, 98, 084028
Cotesta, R., Marsat, S., & Pürrer, M. 2020, PhRvD, 101, 124040
deBoer, R. J., Görres, J., Wiescher, M., et al. 2017, RvMP, 89, 035007
Descouvemont, P., & Baye, D. 2010, RPPh, 73, 036301
Di Carlo, U. N., Giacobbo, N., Mapelli, M., et al. 2019, MNRAS, 487, 2947
Di Carlo, U. N., Mapelli, M., Bouffanais, Y., et al. 2020, MNRAS, 497, 1043
Ebisuzaki, T., Makino, J., Tsuru, T. G., et al. 2001, ApJL, 562, L19
Estellés, H., Husa, S., Colleoni, M., et al. 2021, arXiv:2105.06360
Ezquiaga, J. M., & Holz, D. E. 2021, ApJL, 909, L23
Farmer, R., Renzo, M., de Mink, S. E., Fishbach, M., & Justham, S. 2020, ApJL, 902, L36
Farmer, R., Renzo, M., de Mink, S. E., Marchant, P., & Justham, S. 2019, ApJ, 887, 53
Finn, L. S., & Chernoff, D. F. 1993, PhRvD, 47, 2198
Fishbach, M., & Holz, D. E. 2020, ApJL, 904, L26
Fowler, W. A., & Hoyle, F. 1964, ApJS, 9, 201
Fraley, G. S. 1968, Ap&SS, 2, 96
Fryer, C. L., & Kalogera, V. 2001, ApJ, 554, 548
Gair, J. R., Mandel, I., Miller, M. C., & Volonteri, M. 2011, GReGr, 43, 485
García-Quirós, C., Colleoni, M., Husa, S., et al. 2020, PhRvD, 102, 064002
Gayathri, V., Bartos, I., Haiman, Z., et al. 2020a, ApJL, 890, L20
Gayathri, V., Healy, J., Lange, J., et al. 2020b, arXiv:2009.05461
Gerosa, D., & Berti, E. 2017, PhRvD, 95, 124046
Gialanella, L., Rogalla, D., Strieder, F., et al. 2001, EPJA, 11, 357
Gilmer, M. S., Kozyreva, A., Hirschi, R., Fröhlich, C., & Yusof, N. 2017, ApJ, 846, 100
Graff, P. B., Buonanno, A., & Sathyaprakash, B. S. 2015, PhRvD, 92, 022002
GWOSC 2020, Documentation for O3 Discovery Papers Data Release, https://www.gw-openscience.org/o3_eventdata_docs/
Haster, C.-J., Wang, Z., Berry, C. P. L., et al. 2016, MNRAS, 457, 4499

Heger, A., Fryer, C. L., Woosley, S. E., Langer, N., & Hartmann, D. H. 2003, ApJ, 591, 288
Hunter, J. D. 2007, CSE, 9, 90
Joggerst, C. C., & Whalen, D. J. 2011, ApJ, 728, 129
Khalil, M., Buonanno, A., Steinhoff, J., & Vines, J. 2021, PhRvD, 104, 024046
Kimball, C., Talbot, C., Berry, C. P. L., et al. 2021, ApJL, 915, L35
Kozyreva, A., Yoon, S.-C., & Langer, N. 2014, A&A, 566, A146
Kunz, R., Fey, M., Jaeger, M., et al. 2002, ApJ, 567, 643
Lane, A. M., & Thomas, R. G. 1958, RvMP, 30, 257
Liu, X., Cao, Z., & Zhu, Z.-H. 2021, arXiv:2102.08614
Mapelli, M., Dall'Amico, M., Bouffanais, Y., et al. 2021, MNRAS, 505, 339
Marchant, P., & Moriya, T. J. 2020, A&A, 640, L18
Miller, M. C., & Colbert, E. J. M. 2004, IJMPD, 13, 1
Miller, M. C., & Hamilton, D. P. 2002, MNRAS, 330, 232
Nagar, A., Bonino, A., & Rettegno, P. 2021, PhRvD, 103, 104021
Nitz, A. H., Capano, C., Nielsen, A. B., et al. 2019, ApJ, 872, 195
Nitz, A. H., & Capano, C. D. 2021, ApJL, 907, L9
Nitz, A. H., Dent, T., Davies, G. S., et al. 2020, ApJ, 891, 123
O'Leary, R. M., Rasio, F. A., Fregeau, J. M., Ivanova, N., & O'Shaughnessy, R. 2006, ApJ, 637, 937
Ober, W. W., El Eid, M. F., & Fricke, K. J. 1983, A&A, 119, 61
Ossokine, S., Buonanno, A., Marsat, S., et al. 2020, PhRvD, 102, 044055
Pan, Y., Buonanno, A., Boyle, M., et al. 2011, PhRvD, 84, 124052
Paxton, B., Bildsten, L., Dotter, A., et al. 2011, ApJS, 192, 3
Paxton, B., Cantiello, M., Arras, P., et al. 2013, ApJS, 208, 4
Paxton, B., Marchant, P., Schwab, J., et al. 2015, ApJS, 220, 15
Paxton, B., Schwab, J., Bauer, E. B., et al. 2018, ApJS, 234, 34
Paxton, B., Smolec, R., Schwab, J., et al. 2019, ApJS, 243, 10
Planck Collaboration, Ade, P. A. R., Aghanim, N., et al. 2016, A&A, 594, A13
Portegies Zwart, S. F., & McMillan, S. L. W. 2000, ApJL, 528, L17
Pratten, G., García-Quirós, C., Colleoni, M., et al. 2021, PhRvD, 103, 104056
Quinlan, G. D., & Shapiro, S. L. 1989, ApJ, 343, 725
Rakavy, G., & Shaviv, G. 1967, ApJ, 148, 803
Renzo, M., Farmer, R., Justham, S., et al. 2020, A&A, 640, A56
Rodriguez, C. L., Zevin, M., Amaro-Seoane, P., et al. 2019, PhRvD, 100, 043027
Romero-Shaw, I., Lasky, P. D., Thrane, E., & Calderón Bustillo, J. 2020, ApJL, 903, L5
Sallaska, A. L., Iliadis, C., Champange, A. E., et al. 2013, ApJS, 207, 18
Sathyaprakash, B. S., & Dhurandhar, S. V. 1991, PhRvD, 44, 3819
Schürmann, D., Gialanella, L., Kunz, R., & Strieder, F. 2012, PhLB, 711, 35
Schutz, B. F. 1986, Natur, 323, 310
Skilling, J. 2006, BayAn, 1, 833
Stothers, R. B. 1999, MNRAS, 305, 365
Sukhbold, T., & Woosley, S. E. 2014, ApJ, 783, 10
Sukhbold, T., Woosley, S. E., & Heger, A. 2018, ApJ, 860, 93
Takahashi, K. 2018, ApJ, 863, 153
Timmes, F. X., Woosley, S. E., & Weaver, T. A. 1996, ApJ, 457, 834
Townsend, R. H. D. 2019a, MESA SDK for Linux, 20190503, Zenodo, doi:10.5281/zenodo.2669541
Townsend, R. H. D. 2019b, MESA SDK for Mac OS, 20190503, Zenodo, doi:10.5281/zenodo.2669543
Uberseder, E., & deBoer, R. J. 2015, AZURE2 User Manual, https://azure.nd.edu/documentation.php
Umeda, H., Yoshida, T., Nagele, C., & Takahashi, K. 2020, ApJL, 905, L21
Vallisneri, M., Kanner, J., Williams, R., Weinstein, A., & Stephens, B. 2015, JPhCS, 610, 012021
van der Walt, S., Colbert, S. C., & Varoquaux, G. 2011, CSE, 13, 22
Varma, V., Field, S. E., Scheel, M. A., et al. 2019a, PhRvR, 1, 033015
Varma, V., Field, S. E., Scheel, M. A., et al. 2019b, PhRvD, 99, 064045
Veitch, J., Pürrer, M., & Mandel, I. 2015a, PhRvL, 115, 141101
Veitch, J., Raymond, V., Farr, B., et al. 2015b, PhRvD, 91, 042003
Venumadhav, T., Zackay, B., Roulet, J., Dai, L., & Zaldarriaga, M. 2020, PhRvD, 101, 083030
Woosley, S. E. 2017, ApJ, 836, 244
Woosley, S. E., & Heger, A. 2021, ApJL, 912, L31
Woosley, S. E., Heger, A., & Weaver, T. A. 2002, RvMP, 74, 1015
Yoshida, T., Umeda, H., Maeda, K., & Ishii, T. 2016, MNRAS, 457, 351
Yun, Q., Han, W.-B., Zhong, X., & Benavides-Gallego, C. A. 2021, PhRvD, 103, 124053
Zackay, B., Dai, L., Venumadhav, T., Roulet, J., & Zaldarriaga, M. 2021, PhRvD, 104, 063030
Zhang, W., Woosley, S. E., & Heger, A. 2008, ApJ, 679, 639